Title:

Developmental constraints modulate reproductive fate and plasticity within the Arabidopsis ovule primordium

Elvira Hernandez-Lagana[1]*, Gabriella Mosca[2]*, Ethel Mendocilla Sato[2]*, Nuno Pires[2], Anja Frey[2,4], Alejandro Giraldo-Fonseca[2], Ueli Grossniklaus[2], Olivier Hamant[3], Christophe Godin[3], Arezki Boudaoud[3], Daniel Grimanelli[1], Daphné Autran[1#], Célia Baroux[2#]

Affiliations :

1 Diversité, Adaptation et Développement des Plantes (DIADE), IRD, CIRAD, University of Montpellier, Montpellier, France.

2 Department of Plant and Microbial Biology and Zurich-Basel Plant Science Center, University of Zurich, Zurich, Switzerland.

3 Laboratoire Reproduction et Développement des Plantes, University of Lyon, ENS Lyon, UCB Lyon 1, CNRS, INRAE, INRIA, Lyon, France.

4 Present address: Novartis Pharma Schweiz AG, Basel, Switzerland.

* equal contribution.

authors for correspondence: daphne.autran@ird.fr, cbaroux@botinst.uzh.ch

The authors declare no competing financial interests.

ORCID numbers

Name	Orcid #
Elvira Hernandez-Lagana	0000-0002-2645-3783
Gabriella Mosca	0000-0003-4509-498X
Ethel Mendocilla-Sato	0000-0003-0339-3535
Alejandro Giraldo-	0000-0003-2943-9810
Nuno Pires	0000-0002-7113-3519
Anja Frey	
Ueli Grossniklaus	0000-0002-0522-8974
Olivier Hamant	0000-0001-6906-6620
Arezki Boudaoud	0000-0002-2780-4717
Christophe Godin	0000-0002-1202-8460
Daniel Grimanelli	0000-0001-5424-114X
Daphné Autran	0000-0002-5227-8966
Célia Baroux	0000-0001-6307-2229

Summary

Sexual reproduction in multicellular organisms requires the separation of the germline from the soma. In flowering plants, the formation of spore mother cells (SMCs) marks the somatic-to-reproductive cell fate transition in floral organs. The female SMC differentiates at the apex of the ovule primordium, as a single, large, and elongated subepidermal cell. However, this singleness rule is not very robust: several SMC candidates develop in some *Arabidopsis* accessions and mutants. Yet, the basis of this plasticity is not understood. Here we investigate whether ovule primordium growth and overarching cellular architecture serve as an instructive cue to channel the formation of a single SMC. Combining quantitative analyses of 3D cell-based information, cell cycle reporters, and 2D growth simulations, we provide a comprehensive analysis of cell proliferation and growth events that shape ovule primordium development and SMC formation. This reveals that SMC characteristics emerge earlier than previously thought, and often for more than one cell. Thus, developmental constraints gradually canalize the fate of these cells, so that a single SMC enters meiosis ultimately. Among these constraints, we explore the contribution of dynamic cell division patterns and localized cell growth anisotropy. Consistent with 2D computational simulations, the reduction of anisotropy in *katanin* mutants leads to altered ovule shape and cell division patterns. Such disturbance of ovule morphology is sufficient to delay SMC canalization, as multiple cells express reproductive fate markers in *katanin* mutant ovules. In conclusion, we show that ovule growth and shape channel SMC fate for a single cell.

Highlights

1. SMC singleness emerges from a canalization process mediated by KATANIN.
2. Anisotropic cell growth and local, biphasic cell divisions patterns explain ovule primordium shape.
3. 2D-mechanical growth models relate ovule growth and SMC emergence.
4. A 3D image resource of developing ovule primordia at cellular resolution.

50 ## Introduction

51 A hallmark of sexual reproduction in multicellular organisms is the separation of the germline from the
52 soma. In animals, primordial germ cells (PGCs) are set-aside during embryogenesis from a mass of
53 pluripotent cells. The number of germ cells depends on the balance between proliferation (self-renewal)
54 and differentiation, a process controlled by both intrinsic factors and the surrounding somatic tissue
55 (Extavour and Akam, 2003; Kimble 2011). In flowering plants, by contrast, the spore mother cells
56 (SMCs), representing the germline precursors, differentiate late in development. SMCs arise multiple
57 times, i.e., in each flower during the formation of reproductive organs. In *Arabidopsis*, the female SMC
58 differentiates in the nucellus of the ovule primordium, a digit-shaped organ outgrowing from the
59 placental tissue of the gynoecium. The SMC is recognizable as a single, large, and elongated
60 subepidermal cell, in central position, at the nucellus, and displaying a prominent nucleus and nucleolus
61 (Bowman, 1993, Schneitz *et al.,* 1995, Bajon *et al.*, 1999, Schmidt *et al*., 2015).

62 Although SMC singleness may appear to be robust, more than one SMC candidate per primordium can
63 develop at variable frequencies depending on the *Arabidopsis* accession (9,6% in *Columbia* (*Col-0*), 27%
64 in *Monterrosso* (*Mr-0)*, Rodriguez-Leal *et al.,* 2015). Mutants in *Arabidopsis*, maize, and rice that
65 compromise SMC singleness unveiled the role of regulatory pathways involving intercellular signaling,
66 small RNAs, as well as DNA and histone methylation (Sheridan *et al.*, 1996; Sheridan *et al.*, 1999;
67 Nonomura *et al.*, 2003; Zhao *et al.*, 2008; García-Aguilar *et al.,* 2010; Olmedo-Monfil *et al*., 2010;
68 Schmidt *et al.,* 2011; Su *et al*., 2017; Su *et al.,* 2020). As the SMC forms, cell-cycle regulation contributes
69 to the stabilization of its fate in a cell-autonomous manner through cyclin-dependent kinase (CDK)
70 inhibitors and RETINOBLASTOMA-RELATED1 (RBR1) (Zhao *et al.,* 2017; Cao *et al.*, 2018). SMC singleness
71 thus appears to result from a two-step control: first, restricting differentiation to only one cell and
72 second, preventing self-renewal before meiosis (reviewed in Lora *et al*., 2019, Pinto *et al.*, 2019).

73 However, the precise mechanisms underlying the plasticity in the number of SMC candidates and SMC
74 fate specification are still poorly understood. In principle, SMC singleness may be controlled by
75 successive molecular cues. However, even in that scenario, such cues must be positional, at least to
76 some extent, and thus involve a spatial component. In the last decade, many different molecular cues
77 defining spatial patterns in the ovule primordium were identified (Pinto *et al.*, 2019; Su *et al.,* 2020),
78 however their coordination is unknown. Since SMCs emerge at the primordium apex concomitant with
79 its elongation, we hypothesize that developmental constraints during ovule morphogenesis influence

SMC singleness and differentiation. Such a scenario could explain variation in the number of SMC candidates, ultimately culminating in a single SMC entering meiosis, a process that was previously discussed as a possible canalization (Rodriguez-Leal *et al.*, 2015). Canalization refers to the capacity of an organism to follow a given developmental trajectory in spite of disturbances (Waddington, 1942; Scharloo, 1991, Hallgrimsson *et al.*, 2019). Yet, canalization as proposed by Waddington embraces a broader meaning, including the nature of the developmental process itself to explain phenotypic variability (Waddington, 1942). Answering the questions of whether SMC formation follows a stereotypical or plastic developmental process and whether it is intrinsically linked to or independent of ovule primordium growth would unravel fundamental principles connecting cell fate establishment and organ growth.

Such an analysis requires a high-resolution description of the ovule tissue topology and geometry in time. Our current knowledge of ovule primordium growth in *Arabidopsis* is based on two-dimensional (2D) micrographs from tissue sections or clearings. It is described in discrete developmental stages capturing classes of primordia by their global shape and SMC appearance until meiosis and by the presence of integument layers and ovule curvature later-on (Grossniklaus and Schneitz, 1998). In addition, a 3D analysis of average cell volumes during primordium growth was recently provided (Lora *et al.*, 2017). Yet, we lack a view of the patterning processes shaping the early ovule primordium, the relation of cell layers and proliferation domains in 3D, and a temporally resolved description of primordium emergence. To address the question of SMC singleness, we thus developed a resource where the growth of the ovule primordium is described and quantified at cellular resolution in 3D. We combined 3D imaging, quantitative analysis of cell and tissue characteristics, reporter gene analyses, 2D mechanical growth simulations, and genetic analyses. Using the *katanin* mutant affecting anisotropic cell growth and cell division patterns (Luptovciak *et al*., 2017a, Ovecka *et al*., 2020), we show that an altered ovule morphology is sufficient to disrupt SMC singleness. We also uncovered that differentiation of SMC candidates initiates earlier than previously thought. Finally, we provide evidence for a developmental canalization process leading to the specification of a single SMC prior to meiosis.

Results

Building a reference collection of 3D images capturing developing ovule primordia in 3D at cellular resolution

To generate 3D reconstructions of ovule primordia with cellular resolution at consecutive different stages we imaged primordia stained for cell boundaries in intact carpels by confocal microscopy. Carpels were cleared and stained using a modified PS-PI staining (Truernit *et al*., 2008) and mounting procedure preserving their integrity (Mendocilla-Sato and Baroux, 2017; Figure 1A). We selected high signal-to-noise ratio images and segmented them based on cell boundary signals using a previously described pipeline (Mendocilla-Sato and Baroux, 2017; Figure 1B). We manually curated 92 ovules representing seven consecutive developmental stages (7-21 ovules per stage, Figure 1B, Table 1, Data S1), classified according to an extended nomenclature explained in the STAR Methods. In order to gain temporal resolution, we defined new stages (st0-I to st0-III) covering primordium emergence, which occurs prior to the straight digit-shape organ stage 1-I where the SMC becomes distinguishable by its apparent larger size in longitudinal views (Schneitz and Grossniklaus, 1998).

To evaluate the distinct contribution of domain-, layer- and cell-specific growth dynamics, we assigned a label to each segmented cell enabling data classification (Figure 1B, STAR Methods). We defined cell labels to distinguish *domains*, *layers* and *cell types*: the apical and basal domains, the L1 and L2,L3 layers (L1, epidermis; and the underlying L2 and L3 layers taken together), and seven cell types intersecting with the domains and layers. The latter include the self-explanatory cell labels “L1 apical”, “L1 basal”, “L2,L3 apical”, “L2,L3 basal”, “SMC”, and specific labels for the “L1 dome”, the upmost apical L1 cells in contact with the SMC, and the “CC” or companion cells, the elongated L2 cells adjacent to the SMC.

To quantitatively analyze the data with respect to cell labels, layers, domains, ovule stage and genotype, we developed an interactive, R-based interface named OvuleViz. The script reads cell descriptors exported from segmented image files and enables multiple plot generation from a user-based selection of (sub)datasets (Figure S1A-C, STAR Methods). Collectively, our work generated a reference collection of annotated, 3D images capturing ovule primordium development at cellular resolution from emergence until the onset of meiosis. The collection of 92 segmented images associated with a total of 7763 annotated cells and five morphological cell descriptors (volume, area, sphericity, prolate and oblate ellipticity) provides a unique resource for morphodynamic analyses of ovule primordium growth.

140 To identify correlations between growth patterns and differentiation, we performed a principle
141 component analysis (PCA) based on the aforementioned cell descriptors, *per* cell type and stage,
142 considered together or separately (Figure S1D-E). In this global analysis, the SMC appears distinct at late
143 stages (2-I and 2-II) but clear conclusions are hampered by a crowding effect that is not resolved by this
144 approach. This prompted us to investigate in detail the contribution of different layers, domains, and
145 cell types to ovule primordium growth and in relation to SMC differentiation.
146

147 **Ovule primordium morphogenesis involves domain-specific cell proliferation and anisotropic cell**
148 **shape patterns**
149

150 The ovule primordium emerges from the placenta as a small dome-shaped protrusion and grows into a
151 digit-shaped primordium with nearly cylindrical symmetry (stage 1-I) before enlarging at the base
152 (Figure 1B). Using our segmented images, we first quantified global changes in cell number, cell volume ,
153 and ovule primordium shape. Our analysis revealed two distinct phases of morphological events. Phase I
154 (stages 0-I to 0-III) is characterized by a 4.5-fold increase in total cell number but a moderate increase in
155 mean cell volume (10%, P=0.03). By contrast, Phase II (stages 1-I to 2-II) is characterized by a moderate
156 increase in cell number (50%) and the global mean cell volume is relatively constant (Figure 2A, S2A). To
157 quantify the resulting changes in organ shape, we extrapolated a continuous surface mesh of the ovule
158 outline and used it to compute its height and width at the base (Figure 2B-C, S2B, STAR Methods).
159 Anisotropic organ growth during Phase I was confirmed by a steady increase in height while primordium
160 width increased moderately (Figure 2C). This contrast in morphodynamic events between Phase I and II
161 is illustrated by the representation of fold-changes (FCs) in cell number and aspect ratio (Figure 2D)
162 which range between 1.5 and 2.0 in Phase I whereas drop to 1.4 and 1.2 in Phase II. These observations
163 confirmed that Phase I captures a distinct growth dynamic compared to Phase II.
164 Next, to capture possible specific patterns of growth, we analyzed cell number, cell size, and cell
165 shape using different viewpoints: one comparing the L1 and L2,L3 layers and one contrasting the apical
166 *vs* basal domains. Scoring cell number per viewpoint clearly showed a dominant contribution of the
167 epidermis (L1) relative to the subepidermal layers and of the basal relative to the apical domain (Figure
168 2E,F). To verify these findings with a cellular marker, we analyzed the M-phase-specific *CYCB1.1-dbGFP*
169 reporter (Ubeda-Tomas et al, 2009). We scored the number of GFP-expressing cells among 481 ovules
170 and plotted relative mitotic frequencies *per* cell layer and domain for each ovule stage to generate a
171 cell-based mitotic activity map (Figure 2G-H, Data S2, STAR Methods). In this approach, subepidermal

172 cells beneath the dome were distinguished from underlying L3 cells to gain resolution on the L2 apical
173 domain where the SMC differentiate. Consistent with our previous observation, in Phase I, a high
174 proliferation activity was scored in L1 cells at the primordium apex (scoring 64% of mitotic events). By
175 contrast, the L2 apical domain remains relatively quiescent (contributing only 3% of the mitotic events).
176 During Phase II, proliferation preferentially occurs in the basal domain with > 60% of mitotic events at all
177 stages. It is noteworthy that during this phase, L2 apical cells divide relatively rarely, with the exception
178 of SMC neighbors cells that show frequent divisions at stage 1-II. Thus, reporter analysis confirmed a
179 biphasic, temporal pattern of cell division with changing regional contributions, suggesting the L1 apical
180 and L2,L3 basal domains as consecutive sites of increased proliferation, contributing to morphological
181 changes in Phase I and II, respectively.

182 Cell size analysis, by contrast, did not reveal significant changes during primordium development
183 with the notable exception of the SMC (Figure 2A, S2C). The SMC gradually attains a distinct size starting
184 at stage 0-III when compared to other L2,L3 cells (Figure 2I) or even earlier, at stage 0-I, when compared
185 to all other cells (Figure 2I inset). Size differentiation of the SMC is not uniform among ovules,
186 demonstrating plasticity in the process (Figure S2D). In addition, different cell sizes between L1 and
187 L2,L3 layers are already discernible at primordium emergence (Figure 2J, S2E). The presence of larger
188 L2,L3 cells is consistent with the low division frequency observed previously - likely stemming from
189 longer growth phases. We propose that cell size asymmetry established at early stages favors SMC
190 emergence.

191 We then investigated cell shape changes during primordium elongation, using ellipticity and
192 sphericity indices computed by Imaris (Bitplane, Switzerland) following segmentation. The analysis did
193 not reveal significant differences between domains or layers (Figure S2F, STAR Methods). This could
194 indicate either a highly variable cell shape or more localized, cell type-specific shape changes. We thus
195 more specifically analyzed the subepidermal niche where the SMC differentiates. We found that
196 companion cells (CC) showed an increasing ellipticity (and decreasing sphericity), starting at stage 1-I
197 and culminating at stage 2-I (Figure S2F). By contrast, the SMC only showed a moderate decrease in
198 sphericity at late stages and no distinctive ellipticity at early stages (Figure S2F). In order to get raw
199 information on anisotropy of cells shapes, we developed an extension for MorphoMechanX
200 (www.morphomechanx.org) to (i) perform a semi-automatic labeling of cell layers and cell types from a
201 cellularized mesh and (ii) compute in each 3D cell the principal axes of shape anisotropy and the
202 corresponding indexes (Figure S2G, STAR Methods, Movie S1). The maximum anisotropy shape index of
203 the SMCs was, averaged *per* stage, consistently above the medium (and hence above the minimum)

204 anisotropy index (Figure 2K). This confirmed that the SMC has an anisotropic shape, with a
205 distinguishable major axis throughout ovule primordium development from early stages onwards
206 (Figure S2H). We measured the degree of alignment of the SMC major axis with the main growth axis of
207 the ovule during early stages (stage 0-II) and found a mean angle of 22° (+/- 11°, n=16) (Figure 2K, see
208 also Figure 2C showing main growth axis of the ovule along development). Thus, the SMC's anisotropic
209 shape emerges at the earliest stages and its orientation is aligned with the growth axis of the
210 primordium.

211 Taken together, these results suggest that anisotropic primordium growth is linked to domain-
212 specific cell proliferation combined with localized, anisotropic expansion.

213

214 2D mechanical simulations of ovule primordium development relate its coordinated growth to SMC 215 shape emergence

216 Organ shape is determined by the rate and direction of cell growth, the latter affected by signaling and
217 the mechanical state of the tissue and its geometry, with possible feedback interactions between them
218 (Basel *et al*., 2014, Echevin *et al.*, 2019). Mechanical constraints arise from the growth process in form of
219 tensile and compressive forces that, in turn, influence cell and tissue growth depending on their
220 elastic/visco-plastic properties (Echevin *et al*., 2019). To determine the role of ovule primordium growth
221 on SMC differentiation, which involves early differential cell growth, we sought to understand the
222 contributions of growth rate and anisotropy and their relation to signaling and mechanical constraints
223 (Coen *et al*., 2004; Kenaway *et al*., 2011). Resolving this question would define fundamental
224 developmental principles linking organ growth and SMC differentiation.
225 We first sought to determine morphogenetic principles of primordium growth at the tissue level by
226 developing a 2D Finite Element Method (FEM)-based mechanical model, which considered two
227 uncoupled but complementary modes of growth: (i) signal-based growth in which an abstract
228 morphogen captures the cumulative effects of biochemical signals without considering its explicit mode
229 of action (i.e., cell wall loosening, increase in turgor pressure) (Boudon *et al.*, 2015); and (ii) passive
230 strain-based growth in which relaxation accommodates excess of strain (and therefore also excess of
231 stress) that accumulated in the tissue by relaxing its reference configuration according to the amount of
232 strain. The mechanical equilibrium is computed to ensure compatibility with the tissue that is locally
233 growing at different rates and orientations. This introduces residual internal compressions and tensions
234 to which the action of turgor pressure is also added (Rodriguez *et al.,* 1994). A polarization field is used
235 to set the direction of anisotropic growth for both growth mechanisms (Coen *et al.,* 2004). The

236 simulation consists of iterations where the mechanical equilibrium is computed before each growth step
237 is specified by signal- and strain-based growth. This strategy extends previous tissue growth models
238 (Kuchen *et al*., 2012, Borzog *et al*., 2016, Boudon *et al*., 2015, Mosca *et al.,* 2018, STAR Methods).

239 We designed a starting template consisting of an L1 layer distinct from the underlying L2, L3
240 tissue based on different growth and material properties (Jarrousse, 2014) (Table 2, Figure S3, STAR
241 Methods). We first set the model components to produce a realistic elongated, digit-shaped primordium
242 with a narrow dome and an L1 layer of stable thickness during development (Reference Model, FEM-
243 Model 1) (Figure 3A, S3A). This model combines the following hypotheses: a narrow domain of
244 anisotropic, signal-based growth, a broad domain competent for passive strain-based relaxation and
245 material anisotropy.

246 Then, using the versatility of the modeling framework to vary initial conditions, we asked
247 whether primordium morphogenesis is driven primarily by growth of the epidermis (L1) or if it requires
248 active growth of inner tissues. In the first scenario, L1 growth is responsible for creating a dome shape,
249 enabling underlying tissue growth by pulling on the inner layers and inducing cell divisions as observed
250 in Phase I. In another scenario, active growth of the inner tissues forces the L1 to grow and create a
251 protrusion. We ran several simulations with varying initial distribution patterns of the growth signal
252 (Table 2). The shape aberrations produced by FEM-Models 4, 5, 6 and 7 (Figure S3B) suggested that an
253 inner tissue-driven growth principle (*vs* L1-driven), involving a narrow strip of initial growth signal
254 diffusing in the inner layers, was more plausible (Reference Model, FEM-Model 1, Figure 3A, S3A). Next,
255 through modulation of passive strain-based growth, we determined that a broad tissue domain
256 uniformly competent for strain accommodation is necessary to resolve the high accumulation of strain,
257 limiting primordium elongation (FEM-Model 8, Figure S3C). Yet, material anisotropy influencing the
258 relaxation response is not necessarily required broadly and it is sufficient to specify it in the L1 only to
259 achieve a dome with a realistic shape and constant L1 thickness (FEM-Model 2, Figure S3C). Finally, we
260 asked whether growth anisotropy must be specified in the model or if geometrical and mechanical
261 constraints are sufficient to specify primordium shape. Clearly, removing this component abolished the
262 digit shape of the primordium and produced a hemi-spherical protrusion (FEM-Model 3, Figure 3B).

263 In summary, we identified parsimonious growth principles shaping the ovule primordium: an
264 inner tissue-driven process promoted by a narrow domain of anisotropic, signal-based growth is
265 complemented by passive tissue growth in response to accumulated strain. Furthermore, material
266 anisotropy in the L1 is predicted to play a role in constraining L1 thickness as observed experimentally.

267 Next, we aimed to analyze how cell division and cell shape, particularly that of the SMC, are
268 connected to tissue growth patterns at cellular scale. For this, we developed a complementary model
269 with cellular resolution. This vertex-based model features cells as 2D polygons whose walls are mass
270 spring (MS) segments (Smith, 2009; Amar, 2009). This model integrates mechanics (Hooke's law for MSs)
271 with signal- and strain-based growth as before (STAR Methods). We simulated growth starting with a
272 virtual grid of cells representing a flat placenta and focused on early stages of ovule primordium
273 formation until stage 1-I. We tested the same combination of growth hypotheses as for the continuous
274 model (Table 2), except for material anisotropy that cannot easily be embedded in a vertex-based
275 model. As we observed that L1 cells do not divide periclinally, nor change in volume on average, we
276 deduced that their growth occurs mainly in direction of the main axis of the primordium. For this reason,
277 we enforced this feature in our model, preventing growth of the anticlinal walls (both for signal-based
278 growth and passive strain-based growth, STAR Methods). This constraint limits the ways an organ can
279 grow in a digit-shaped fashion, as the L1 does not progressively populate the inner tissues by division.
280 Furthermore, our models included assumes a slower division rate for L2,L3 apical cells, consistent with
281 our previous observations (Figure S3D).
282 We identified MS-Model 2 to best capture the characteristic shape and aspect ratio of ovules
283 (Figure 3C, S3D). This reference model confirmed the growth hypotheses from FEM-based simulations
284 regarding the distribution and orientation of signal-based growth (Figure S3B) and passive strain-based
285 growth (Figure S3C).
286 Finally, we were interested to determine whether SMC morphology is an emerging property of
287 primordium growth and how anisotropic growth influences the process. Remarkably, in the cell-based
288 reference model including anisotropic cell growth, an SMC candidate emerged early: a central L2 apical
289 cell that, beside its larger size, adopted a trapezoidal shape and a principal anisotropy axis aligned with
290 the main direction of ovule growth (Figure 3E). Such features are qualitatively comparable what we
291 observed for stage 0-II primordia (Figure 3E, S3D, Figure 2K).
292 The MS-Model 3 corresponds to a virtual mutant with isotropic cell growth. Under these
293 conditions, ovule primordia displayed an altered shape with a wider surface and flatter dome as in the
294 FEM-Model 3 (Figure 3D). Interestingly, a larger, central L2 cell still emerged but the elongated shape
295 typical of SMCs arose later in the simulation progression as compared to the reference model (Figure 3F,
296 Movie S3). Thus, 2D simulations predict that anisotropic cell growth does not only affect ovule
297 primordium shape but also the timing of SMC candidate emergence, hence connecting the growth
298 process with SMC differentiation. In these models, the candidate SMC eventually divided as they missed

299 a causative rule to differentially regulate cell division. When we prevented the SMC candidate to divide,
300 its enlargement overrode primordium shape control in our simulations, indicating an additional level of
301 control in real primordia (Figure S3E).

302 Altogether, the two complementary growth models of ovule primordium development confirm
303 at different scales a role for regional cell growth compatible with previous observations. They predict
304 that tissue accommodation, anisotropy in mechanical properties, and a specific pattern of signal-based
305 growth collectively influence the directional growth of the primordium. We showed that altered ovule
306 primordium growth affects size and shape of the SMC candidate, linking organ architecture to SMC fate.
307 Reciprocally, unleashing SMC growth leads to deformation of the primordium, suggesting the existence
308 of a compensatory feedback mechanism that coordinates cell and organ growth.

309

310 *katanin* mutants show a distinct ovule primordium architecture primarily through altered cell division 311 patterns

312

313 To test the model predictions experimentally, we analyzed the consequences of cell growth anisotropy
314 perturbation on ovule primordium growth and SMC fate establishment. *Arabidopsis* plants carrying a
315 defective microtubule-severing protein KATANIN exhibit organ shape defects, including increased round-
316 and bumpiness, as a consequence of disorganized cortical microtubules and isotropic cellulose
317 microfibril orientations (Bichet et al 2001, Burk et al 2002). We thus analyzed the shape and cellular
318 organization of ovule primordia in *katanin* mutants using the *botero* (*bot1-7*) (*Ws* background), *lue1*, and
319 *mad5* alleles (*Col* background) (Bichet *et al*., 2001; Bouquin *et al*., 2003; Brodensen *et al*., 2008),
320 collectively referred to *katanin* (*kat*) mutants hereafter. We generated and analyzed a new dataset of 59
321 annotated 3D digital *kat* and corresponding wild-type ovule primordia at stages 0-III, 1-I, and 1-II (Data
322 S4a). *kat* mutant primordia have an increased size and a more isotropic shape (Figure 4A), being 1.5
323 times bigger in volume than wild-type primordia (P=0.007, stage 0-III, Figure 4B) with a smaller aspect
324 ratio (P<0.01 stages 1-I, 1-II, Figure 4C). The width-to-height aspect ratio does not inform on the shape
325 at the flanks, hence does not discriminate straight digit *versus* plump organ shapes. We estimated the
326 "plumpiness" of the primordia by calculating the volume fraction of a fitting, 3D parallelepiped
327 (bounding box) effectively occupied by the primordium (bounding box occupancy, Figure 4D, S4A). In *kat*
328 ovules, the relationship deviates from the wild type beginning at stage 1-I, when the primodium
329 normally starts elongating along the major growth axis. These measurements confirmed a marked
330 attenuation of anisotropic growth in *kat* primordia as was observed in roots, shoot organs, or seeds
331 (Bichet *et al*., 2001; Uyttewaal *et al.,* 2012, Hervieux *et al*., 2016; Ren *et al*., 2017; Wigthman *et al*., 2013;

332 Zhang et al 2013; Luptovciak et al 2017b). Yet, at a global level, the mean cell number, cell volume, and
333 sphericity are not significantly different between *kat* and wild-type primordia (Figure S4B). Thus, these
334 global approaches did not resolve the origin of primordia mis-shaping.

335 To refine the analysis, we contrasted different layers as done for wild-type primordia and found
336 local alterations that provide an explanation for the formation of broader and more isotropic primordia
337 in *kat* mutants. Notably, the epidermis of *kat* primordia contains 17.5% more cells (47 L1 cells in *kat* vs
338 40 in wild-type at stage 0-III, P=0.03). Also, *kat* epidermal cells have a 20% larger volume than in the wild
339 type (P<0.001). Early in development (stage 0-III), the apical domain of *kat* primordia is populated by
340 larger (17%, P<0.001), more spherical (2%, P<0.001) cells than in wild type (Figure 4E,SC), a
341 characteristic that extends to the basal domain at later stages (Figure S4D). To determine whether, in
342 *kat* primordia, the mitotic domains shifted in space and/or time, we scored *CYCB1.1-dbGFP* signals *per*
343 stage, layers, and equivalent domains as before, and expressed it as fold-changes relative to wild-type
344 primordia (Figure 4F, S4E). In Phase I (stage 0-II), we consistently scored 2.4 times less mitoses in the L1
345 dome domain, and 2.7 times more mitoses at the L1 basal domain of *kat* primordia. Hence, in *kat*
346 primordia, proliferation is mostly localized in the basal region and not higher in the early L1 dome as in
347 the wild type.

348 To elucidate whether these alterations affected the cellular domain where the SMC normally
349 differentiates, we interrogated L2 apical cells and specifically the L2 neighbors of the candidate SMC. At
350 stage 0-II, we scored 3.5 times more divisions in the L2 SMC neighbor cells in the apical domain, showing
351 that the relative mitotic quiescence is lost in this domain in *kat* primordia. Next, we focus on cells in
352 contact with the SMC (STAR methods). We found that in *kat* primordia, in contrast to wild-type and to
353 non-neighbor cells, SMC neighbors specifically enlarge as early as stage 0-III (Figure 4G, S4E) but without
354 a detectable increase in sphericity. Consistently, our *CYCB1.1-dbGFP* analysis showed that the mitotic
355 activity detected in SMC neighbors at stage 1-II in wild-type primordia significantly decreases in *ka*t
356 primordia (Figure 4F, S4E).

357 In conclusion, the absence of *KAT*-mediated cell growth anisotropy is associated with major
358 changes in the domains of cell division, which can be linked to geometric changes or to a slow-down of
359 mitosis as previously shown in *kat* mutants (Ovecka *et al*., 2020; Komis *et al*., 2017). These alterations
360 impact ovule primordium shape but also architecture of the subepidermal apical domain, where the
361 SMC differentiates.

362

363 **Altered ovule primordium architecture in *katanin* mutants induces ectopic SMC fate**
364

365 We next investigated whether *kat* ovule growth defects also affect cell identity and SMC singleness. In
366 *kat* primordia, SMCs appear bigger in volume and more spherical than their wild-type counterparts at
367 stage 0-III; yet, no significant differences were detected at stages 1-I and 1-II. However, we observed
368 variability in volume at these stages (Figure 4G, S5A-B). When we analyzed the number of SMC
369 neighbors (Figure 5A-B), we found seven or more in *kat* primordia compared to an average of five in the
370 wild type. The *kat* SMC neighbors were 14% larger (P=0.006), 11% less ellipsoid (P=0.03), and 2% more
371 spherical (P<0.01) than in the wild type (Figure 5B), reminiscent of mutants affecting SMC singleness
372 (Pinto *et al*., 2019).
373 To analyze the identity of these additional, enlarged cells, we quantified several SMC hallmarks.
374 First, we found that ~ 35% *kat* primordia harbor more than one SMC candidate at stage 1-II, decreasing
375 to 14.42% at stage 2-II (Figure 5C). Then, we assessed two complementary markers associated with SMC
376 fate in *kat* primordia. The first marker is a GFP-tagged linker histone variant (H1.1-GFP) that marks the
377 somatic-to-reproductive fate transition by its eviction in the SMC at stage 1-I (She *et al*., 2013): H1.1-GFP
378 eviction occurred in more than one cell in 28.57% *kat* primordia (n=43, Figure 5D). The second marker
379 reports expression of the *KNUCKLES* transcription factor (KNU-YFP) expressed in the SMC (Tucker *et al*.,
380 2012). Detectable as early as stage 1-I in the wild type, it was ectopically expressed in 21% *kat* primordia
381 at stage 1-II (n=43) (Figure 5E, S5B). To test whether the ectopic SMC candidates have a meiotic
382 competence, we analyzed the AtDMC1-GUS reporter (Agashe *et al.*, 2002, Klimyuk and Jones, 1997), and
383 indeed scored ectopic expression in 57% of *kat* primordia (n=56) (Figure 5F). We also analyzed the
384 pWOX2-CenH3-GFP marker labeling centromeres starting at the functional megaspore stage (De Storme
385 *et al.*, 2016) and found 20.7% *kat* primordia (n=29) with two labeled cells, as compared to 3,8% (n=26) in
386 the wild type (Figure S5C).
387 Taken together, these results show that ectopic, abnormally enlarged SMC neighbors in *kat*
388 primordia show at least some characteristics of SMC and/or functional megaspores and can thus adopt a
389 reproductive fate.
390

391 **The growth of a single SMC emerges from a canalization process**

392 Based on our analysis of *kat* primordia, it appeared that the frequency of ectopic SMC candidates was
393 high at early stages but decreased over time. This is reminiscent of the phenotypic plasticity in SMC
394 differentiation observed, to a lesser degree, in different *Arabidopsis* accessions (Rodríguez-Leal *et al*,

395 2015). To characterize this plasticity during development we analyzed 1276 wild-type primordia from
396 stage 0-II to 2-II and scored the number of primordia with one or two enlarged, centrally positioned,
397 subepidermal cells (class A and B, respectively, Figure 6A-C). In the wild type, the majority of primordia
398 showed a single candidate SMC (class A) at the stage 0-II, but 27% primordia (n=289) had two SMC
399 candidates (class B), this frequency decreasing to 3% at stage 2-II (n=103). This finding is consistent with
400 ~ 5% primordia at stage 1-II showing H1.1-GFP eviction (n=43) and KNU-YFP expression (n=88) in more
401 than one cell, respectively (Figure 5D-E).

402 Next, we quantified class A and B primordia in *kat* mutants by scoring 2587 ovules of three
403 alleles (Figure 6C, S6A). Clearly, the canalization process is delayed in *kat* mutant primordia with 33%
404 class B primordia at stage 1-II (n=113) compared to 12% in the wild type (n=281). Consistently, the two
405 previously used SMC markers are observed in ectopic cells in *kat* primordia already at stage 1-I (Figure
406 S6B-C), and more significantly at stage 1-II (28.5% ectopic eviction of H1.1-GFP and 21% ectopic
407 expression of KNU-YFP, Figure 5D-E). At stage 2-II, when 17% of cleared *kat* primordia (n=110) showed
408 ectopic SMCs, H1.1-GFP eviction and KNU-YFP expression was only found in 8% (n=25) and 6.7% (n=74)
409 of the primordia, respectively (Figure S5B-C). Therefore, developmental canalization is not only delayed
410 in *kat* ovules, but there is also a partial uncoupling of cellular morphology and marker expression.

411 Another outcome of this study is the early emergence of SMCs, confirming our former 3D cell-
412 based analysis that showed heterogeneity in cell volume of the L2,L3 apical cells already at stages 0-I/0-
413 II (Figure 2J). To corroborate this finding using a different criterion, we measured the nuclear area,
414 which is a distinctive feature of SMCs (She *et al.,* 2013; Rodriguez-Leal *et al.,* 2015). We compared the
415 nuclear area of SMC candidate to that of surrounding L1 and L2 cells in both class A and B primordia at
416 stages 0-II and 0-III. Wild-type class A and B primordia showed an enlarged nucleus in the candidate
417 SMCs from stage 0-II onwards. This correlation was also true in *kat* primordia, where SMC candidates
418 also showed a 1.37-fold increase in nuclear size compared to the wild type (Figure 6D, S6D-F).

419 The commitment to SMC fate is difficult to resolve at early stages due to the lack of molecular
420 markers. Building on our previous findings, we rationalized that cells from the L2 apical domain with a
421 low frequency of mitotic events could have started to transit toward S-phase. To learn more about cell
422 cycle progress in this domain, we analyzed a GFP-tagged PCNA variant marking the replication
423 machinery (Yokoyama *et al*., 2016). When engaged at active replication forks, PCNA-GFP shows nuclear
424 speckles characteristic of S-phase (Strzalka and Ziemienowicz, 2011). By contrast, it remains in the
425 nucleoplasm in G1- and G2-phase and is undetectable in M-phase. We quantified the nuclear
426 distribution patterns of PCNA-GFP in cells from the L2 apical domain in wild type and *kat* primordia

427 separately for class A and B ovules (Figure 6E-H). At stages 0-II and 0-III, PCNA-GFP was always
428 detectable in both classes, indicating that L2 apical cells are rarely in M-phase, consistent with the
429 *CYCB1.1-dbGFP* marker analysis. Although the majority of class A and B ovules at these stages showed a
430 nucleoplasmic pattern, a significant proportion exhibited the speckled S-phase pattern (Figure 6F). At
431 stage 0-II, 24% of class A ovules (n=112) showed the S-phase pattern in a single, centrally positioned
432 apical cell (candidate SMC), reaching nearly 40% at stage 0-III (n=79) (Figure 6F). Conversely, SMC
433 neighbors rarely showed the S-phase pattern (2 to 5%). In class B ovules, 30% (n=41) and 28% (n=60) at
434 stages 0-II and 0-III, respectively, exhibited the S-phase pattern in at least one of the cells in the apical
435 domain (Figure 6F). Together with our analysis of the *CYCB1.1-dbGFP* marker, these data suggest a
436 prolonged S-phase in SMC candidates in Phase I (stages 0-II, 0-III). Although it is not possible to resolve
437 mitotic *versus* meiotic S-phase, it is tempting to speculate that this is typical for the latter.

438 At the onset of Phase II, PCNA-GFP showed a nucleoplasmic pattern in the SMC of class A ovules
439 and in the L2 apical cells of class B ovules (Figure 6G-H, S6G-H). This is consistent with the detection of
440 newly replicated DNA in the SMC at stage 1-I (She *et al.,* 2013). In contrast to the SMC, the SMC
441 neighbors display the S-phase pattern (Figure 6G-H), consistent with the late divisions reported for these
442 cells in Phase II (Figure 2D). In *kat* primordia, we found an higher frequency of S-phase patterns in SMC
443 candidates in both class A and B ovules in Phase II (Figure 6H, S6F-G) and a lower frequency for SMC
444 neighbors in class A ovules at stages 1-I and 1-II, consistent with the deregulation of *CYCB1.1-dbGFP* in
445 these cells in *kat* primordia.

446 Collectively, our data indicate a cellular heterogeneity in the L2 apical domain that leads to the
447 emergence of one or several SMC candidates as early as stage 0-II. The gradual decrease in the number
448 of primordia with ambiguous SMC candidates suggests developmental canalization associated with a
449 cell-cycle progression, cellular elongation, and robust expression of SMC fate markers. In *kat* primordia
450 displaying architecture alterations, SMC singleness is largely disrupted: the selection of a single SMC is
451 significantly delayed and several SMC candidates persist in an ambiguous cell fate state.
452

453 **Discussion**
454

455 Organogenesis involves coordinated cell division and cell expansion, complex growth processes
456 orchestrated by biochemical and mechanical cues (Echevin *et al.*, 2019). How cell differentiation is
457 coordinated in space and time during organ growth and whether these processes are interrelated are
458 core questions for the elucidation of patterning principles (Whitewoods and Coen, 2017).

459 Here, we tested the hypothesis that ovule primordium growth and overarching organ
460 architecture determines the differentiation of a single SMC, the precursor cell of the female germline,
461 *per* primordium. We established a reference collection of images capturing ovule primordia in 3D at
462 cellular resolution to study how SMC cell fate relates to organogenesis in space and time. This reference
463 set populates a growing number of 3D-segmented images of plant tissues and organs, produced as
464 described here or with new tools for automated analyses (Wolny *et al.*, 2020). This is a pre-requisite to
465 generate a developmental atlas that will integrate organ morphology at cellular resolution and gene
466 expression (Hartmann *et al*., 2020).

467 We report on an exhaustive morphodynamic analysis at cellular resolution, *per* stage, domain,
468 layer, and cell type of the ovule primordium. In combination with reporter gene analyses in wild-type
469 and mutant ovules and tissue growth simulations, this approach aims to elucidate fundamental
470 patterning principles. We found that cell division is not uniformly distributed in space and time and
471 follows a biphasic pattern where proliferation frequencies in L1 and L2,L3 domains alternate between
472 Phases I and II to shape the primordium. Strikingly, the L2 apical domain shows a low mitotic activity in
473 Phase I (stages 0-II, 0-III) with a prolonged S-phase in the SMC candidate. This is reminiscent of the
474 animal germline, where mitotic quiescence is a prerequisite to initiate meiosis (Kimble, 2011; Reik and
475 Surani, 2015) and suggests a functional analogy between the L2,L3 apical domain in ovule primordia and
476 the primordial germline niche in animals. Subsequently, the onset of Phase II coincides with the marked
477 elongation and mitotic quiescence of the SMC, contrasting with active divisions in the basal domain.
478 Thus, the fate of the SMC may be uncoupled early from that of the surrounding cells.

479 Tissue growth simulations allowed us to test the role of three main factors contributing to ovule
480 primordium patterning: i) anisotropic cell growth, ii) spatially confined specified growth signal along the
481 ovule axis, and iii) passive strain–based growth (*i.e.* the baseline competency of the tissue to
482 accommodate to accumulated strain, independently of growth signal). Omitting any of these factors, the
483 resulting models failed to shape a realistic primordium. In particular, isotropic growth produces
484 hemispheric instead of digit-shaped primordia with a flat dome resembling *kat* primordia, in which
485 anisotropic cell growth is altered (Luptovciak *et al*., 2017a). Thus, the *kat* mutant phenotype provides an
486 *in planta* confirmation of our theoretical models. Furthermore, the observation that abnormally shaped
487 *kat* primordia contain cells with ectopic expression of SMC fate markers is consistent with the
488 hypothesis that organ growth and ovule primordium architecture control SMC differentiation.

489 Moreover, our results highlight the developmental constraints for differentiation of a single SMC
490 corresponding to a canalization process. The formation of a single SMC prevails in most angiosperms

491 (Huang and Russell, 1992). Yet, some *Arabidopsis* accessions develop ovule primordia with multiple SMC
492 candidates but ultimately only one SMC is committed to meiosis (Grossniklaus and Schneitz, 1998;
493 Rodriguez-Leal *et al.*, 2015). Our quantifications in two reference accessions (Col-0, Ws) suggest that
494 natural variation affects the timing of the canalization process. Canalization, referring to a progressive
495 constraint of cell fate choice, is well studied in animal systems where it is modulated by intercellular
496 signal-based feedback mechanisms (Heitzler and Simpson, 1991) and epigenetic regulation (Pujadas and
497 Feinberg, 2012). Possibly, the epigenetic and signal-based processes known to regulate SMC
498 differentiation (Lora *et al.*, 2019, Pinto *et al*., 2019) also operate in SMC fate canalization. In addition,
499 the contribution of morphogenetic processes on cell fate specification was recently re-evaluated in the
500 light of tissue mechanics and patterning processes (Chan *et al.,* 2017). Our results are consistent with a
501 role of primordium growth constraints on SMC fate canalization. Possibly, the prolonged cell cycle of
502 subepidermal cells in Phase I leverages competitive cell growth on which canalization can operate.
503 Under this scenario, disturbance of growth homeostasis as in *kat* mutants would render this process
504 ineffective and lead to a higher frequency of primordia with unresolved SMC candidates, unveiling a
505 coupling of SMC fate canalization with organ growth (Figure 6I). De-canalization observed in *kat* mutants
506 is consistent with recent work in *Drosophila* embryos showing that organ shape contributes to
507 developmental canalization (Huang *et al.,* 2020). Interestingly, the formation of a broader dome in *kat*
508 ovule coincides with the formation of a broader inner domain with more cells with an unresolved SMC
509 fate. This is reminiscent of the shoot apical meristem where the shape of the dome correlates with the
510 size and position of domains expressing stem cell regulators, such as WUSCHEL and CLAVATA3 (Gruel *et*
511 *al.,* 2016).

512 Epidermal growth controls shoot apical meristem and shoot growth through the modulation of
513 the expression domains of key regulators in the underlying layers (Savaldi-Goldstein *et al.*, 2007; Gruel
514 *et al.,* 2016). Whether growth of the epidermis similarly controls the cell cycle and SMC fate regulators
515 in underlying layers of ovule primordia is an exciting question for future investigation, particularly
516 considering the role of mechanical constraints on gene regulation (Landrein *et al.*, 2015; Fal *et al.*, 2017).
517 Reciprocally, the role of the underlying layers for epidermis growth and dome shape remains to be
518 determined. Our ovule growth simulations predicted a role for inner tissue-driven growth, similar to
519 what has been proposed for the emergence of leaf primordia (Peaucelle *et al.*, 2011), although this
520 remains debated (Boudon *et al.*, 2015). Moreover, our simulations suggested that passive strain-based
521 growth in the L1 is necessary to achieve a normal primordium shape, and that anisotropic material
522 properties in this layer are required to constrain the relaxation along the main axis of the primordium. A

523 possible explanation for this is the requirement to resolve mechanical conflicts arising between tissue
524 layers that grow at different rates (Hervieux *et al.*, 2016). This would be consistent with the high
525 proliferation activity in the L1 dome at a stage of marked differential growth of the SMC. In this
526 scenario, divisions in L1 may release the mechanical stress generated by SMC growth, leading to
527 anisotropic organ growth. Consistent with this idea, we observed that reduced organ shape anisotropy
528 in *kat* ovules is associated with fewer divisions in the L1 dome. The higher division rate in the wild type
529 might confer higher flexibility for the L1 to bend and follow an anisotropic growth profile driven by the
530 inner layers. By contrast, in *katanin*, non-dividing and elongated cells in the L1 would be expected to
531 transmit higher tension preventing bending. Experimental alterations of properties in L1 or L2,L3 cells,
532 together with 3D modeling, would be required to explore such scenarios.
533 Cell-based models suggested that blocking divisions in the SMC enables it to grow and push on
534 the surrounding cells, affecting significantly the ovule morphology. Therefore, we speculate that, in
535 order to maintain ovule growth homeostasis, differential SMC growth must adapt to the constraints
536 provided by surrounding cells. A gradual reduction of SMC turgor pressure may provide a plausible
537 cause to limit SMC size and maintain correct ovule anisotropy. Due to the limitations of 2D MS-based
538 models, such predictions will need to be tested in 3D cell-based models able to properly reproduce a
539 mechanical scenario for a growing ovule primordium. Nonetheless, this prediction paves the way to
540 further investigate the potential role of turgor pressure gradients across a field of cells, which could
541 provide positional information through the directional movement of water and other molecules,
542 thereby linking organ growth homeostasis, cell growth, and cell fate (Long *et al.*, 2020; Beauzamy *et al.*,
543 2014). Such mechanisms could participate in defining the specific pattern of a growth signal predicted by
544 our simulations. However, the nature of the growth signal(s) and the mechanism(s) establishing its
545 pattern in the placenta prior to primordium emergence remain to be identified. Candidate signals may
546 be the many differentially localized hormones, gene products, and small RNAs known to affect ovule
547 primordium growth (Pinto *et al.*, 2019, Su *et al.*, 2020). For example, in Phase II, auxin responses are
548 restricted to the L1 dome while cytokinin signaling is confined to a region basal to the SMC (Bencivenga
549 *et al.*, 2012). Whether this pattern is established already in Phase I and plays a causative role in
550 primordium patterning and SMC differentiation remains to be determined.
551
552

553 ## Author contributions

554 CB, DA, GM, EHL, DG, OH, AB, CG: Conceptualization; EHL, GM, CB, DA, OH, AB, CG, DG: Methodology;
555 GM, NP, AG: Softwares; EHL, GM, EMS, DA, CB: Validation; EHL, GM, AG, DA, CB: Formal analysis; EHL,
556 EMS, DA, CB: Investigation; EMS, AF, OH: Ressources; EHL, GM, NP, DA, CB: Data curation; EHL, GM,
557 EMS, DG, DA, CB: Writing – Original Draft; EHL, GM, OH, AB, CG, UG, DG, DA, CB: Writing – Reviewing
558 and Editing; EHL, GM, DA, CB: Visualization; CB, DA, DG, OH, AB, UG: Supervision; CB, DA, DG: Project
559 administration; CB, DA, DG, OH, AB, CG, UG: Funding Acquisition. All authors reviewed and revised the
560 manuscript.

561 ## Data availability

562

563 All materials, scripts and datasets generated and analyzed in the current study are available at
564 repositories (see Star Methods) or from the corresponding authors upon reasonable request.

565 ## Acknowledgments

566 We thank S. Strauss (Max Planck Institute for Plant Breeding Research, Cologne, Germany) and B. Lane
567 (John Innes Centre, Norwich, U.K.) for providing code and assessment for mesh generation and
568 simulations; S. Guyer (Bitplane, Switzerland) and M. Lartaud (CIRAD, France) for their help with IMARIS
569 analyses; O. Leblanc (IRD Montpellier, France) for his help with data visualization in R; Montpellier Rio
570 Imaging and the Center for Microscopy and Image Analysis of the University of Zurich for microscopy
571 imaging infrastructures; M. Ueda (Nagoya University, Japan), I. Siddiqi (Center for Cellular and
572 Molecular Biology, India), N. de Storme (Katholieke Universiteit Leuven, Belgium), S. Matsunaga (Tokyo
573 Science University, Japan), M. Tucker (University of Adelaide, Australia), and the NASC stock center for
574 seed germplasms.

575 This work was funded by the University of Zurich, IRD, and a PRCI grant from the Agence Nationale de la
576 Recherche/Swiss National Science Foundation (n°ANR-16-CE93-0002-01 to 04) to CB and DA; a grant
577 from the Swiss National Science Foundation (n° 310030B_160336) to UG, a CONACYT fellowship
578 (n°438277) to EHL, and a fellowship from the Forschungskredit of the University of Zurich (n°FK-74502-
579 04-01) to GM.

580

581 ## References

582 Agashe, B., Prasad, C.K., and Siddiqi, I. (2002). Identification and analysis of DYAD: a gene required for meiotic
583 chromosome organisation and female meiotic progression in Arabidopsis. Development 129, 3935-3943.
584 Amar, M.B.G., A.; M√°ller, M.M.; Cugliandolo, L. (2011). New Trends in the Physics and Mechanics of Biological
585 Systems, Volume 92, (Oxford: Oxford University Press).
586 Bajon, C.H., C.; Motomayor, J.C.; Sauvanet, A.; Robert D. (1999). Megasporogenesis in Arabidopsis thaliana L.: an
587 ultrastructural study. Sexual Plant Reproduction 12, 99-109.
588 Beauzamy, L., Nakayama, N., and Boudaoud, A. (2014). Flowers under pressure: ins and outs of turgor regulation in
589 development. Ann Bot 114, 1517-1533.
590 Bencivenga, S., Simonini, S., Benkova, E., and Colombo, L. (2012). The transcription factors BEL1 and SPL are
591 required for cytokinin and auxin signaling during ovule development in Arabidopsis. Plant Cell 24, 2886-2897.
592 Bichet, A., Desnos, T., Turner, S., Grandjean, O., and Hofte, H. (2001). BOTERO1 is required for normal orientation
593 of cortical microtubules and anisotropic cell expansion in Arabidopsis. Plant J 25, 137-148.
594 Boudon, F., Chopard, J., Ali, O., Gilles, B., Hamant, O., Boudaoud, A., Traas, J., and Godin, C. (2015). A
595 computational framework for 3D mechanical modeling of plant morphogenesis with cellular resolution. PLoS
596 Comput Biol 11, e1003950.
597 Bouquin, T., Mattsson, O., Naested, H., Foster, R., and Mundy, J. (2003). The Arabidopsis lue1 mutant defines a
598 katanin p60 ortholog involved in hormonal control of microtubule orientation during cell growth. J Cell Sci 116,
599 791-801.
600 Bowman, J.L.e. ed. (1993). Arabidopsis: an Atlas of Morphology and Development. (Berlin & New York: Springer-
601 Verlag).
602 Bozorg, B., Krupinski, P., and Jonsson, H. (2016). A continuous growth model for plant tissue. Phys Biol 13, 065002.
603 Brodersen, P., Sakvarelidze-Achard, L., Bruun-Rasmussen, M., Dunoyer, P., Yamamoto, Y.Y., Sieburth, L., and
604 Voinnet, O. (2008). Widespread translational inhibition by plant miRNAs and siRNAs. Science 320, 1185-1190.
605 Burk, D.H., and Ye, Z.H. (2002). Alteration of oriented deposition of cellulose microfibrils by mutation of a katanin-
606 like microtubule-severing protein. Plant Cell 14, 2145-2160.
607 Cao, L., Wang, S., Venglat, P., Zhao, L., Cheng, Y., Ye, S., Qin, Y., Datla, R., Zhou, Y., and Wang, H. (2018).
608 Arabidopsis ICK/KRP cyclin-dependent kinase inhibitors function to ensure the formation of one megaspore
609 mother cell and one functional megaspore per ovule. PLoS Genet 14, e1007230.
610 Chan, C.J., Heisenberg, C.P., and Hiiragi, T. (2017). Coordination of Morphogenesis and Cell-Fate Specification in
611 Development. Curr Biol 27, R1024-R1035.
612 Coen, E., Rolland-Lagan, A.G., Matthews, M., Bangham, J.A., and Prusinkiewicz, P. (2004). The genetics of
613 geometry. Proc Natl Acad Sci U S A 101, 4728-4735.
614 De Storme, N., Keceli, B.N., Zamariola, L., Angenon, G., and Geelen, D. (2016). CENH3-GFP: a visual marker for
615 gametophytic and somatic ploidy determination in Arabidopsis thaliana. BMC Plant Biol 16, 1.
616 Echevin, E., Le Gloanec, C., Skowronska, N., Routier-Kierzkowska, A.L., Burian, A., and Kierzkowski, D. (2019).
617 Growth and biomechanics of shoot organs. J Exp Bot 70, 3573-3585.
618 Extavour, C.G., and Akam, M. (2003). Mechanisms of germ cell specification across the metazoans: epigenesis and
619 preformation. Development 130, 5869-5884.
620 Fal, K., Asnacios, A., Chaboute, M.E., and Hamant, O. (2017). Nuclear envelope: a new frontier in plant
621 mechanosensing? Biophys Rev 9, 389-403.
622 Garcia-Aguilar, M., Michaud, C., Leblanc, O., and Grimanelli, D. (2010). Inactivation of a DNA methylation pathway
623 in maize reproductive organs results in apomixis-like phenotypes. Plant Cell 22, 3249-3267.
624 Grossniklaus, U., and Schneitz, K. (1998). The molecular and genetic basis of ovule and megagametophyte
625 development. Semin Cell Dev Biol 9, 227-238.

626 Hallgrimsson, B., Green, R.M., Katz, D.C., Fish, J.L., Bernier, F.P., Roseman, C.C., Young, N.M., Cheverud, J.M., and
627 Marcucio, R.S. (2019). The developmental-genetics of canalization. Semin Cell Dev Biol 88, 67-79.
628 Hartmann, J., Wong, M., Gallo, E., and Gilmour, D. (2020). An image-based data-driven analysis of cellular
629 architecture in a developing tissue. Elife 9.
630 Heitzler, P., and Simpson, P. (1991). The choice of cell fate in the epidermis in Drosophila. Cell 22, 1083-1092.
631 Hervieux, N., Dumond, M., Sapala, A., Routier-Kierzkowska, A.L., Kierzkowski, D., Roeder, A.H., Smith, R.S.,
632 Boudaoud, A., and Hamant, O. (2016). A Mechanical Feedback Restricts Sepal Growth and Shape in Arabidopsis.
633 Curr Biol.
634 Hong, L., Dumond, M., Zhu, M., Tsugawa, S., Li, C.B., Boudaoud, A., Hamant, O., and Roeder, A.H.K. (2018).
635 Heterogeneity and Robustness in Plant Morphogenesis: From Cells to Organs. Annu Rev Plant Biol 69, 469-495.
636 Huang, A., Rupprecht, J.F., and Saunders, T.E. (2020). Embryonic geometry underlies phenotypic variation in
637 decanalized conditions. Elife 9.
638 Huang, B.Q.R., S.D. (1992). Female Germ Unit: Organization, Isolation, and Function. International Review of
639 Cytology 140, 233-293.
640 Kennaway, R., Coen, E., Green, A., and Bangham, A. (2011). Generation of diverse biological forms through
641 combinatorial interactions between tissue polarity and growth. PLoS Comput Biol 7, e1002071.
642 Kimble, J. (2011). Molecular regulation of the mitosis/meiosis decision in multicellular organisms. Cold Spring Harb
643 Perspect Biol 3, a002683.
644 Klimyuk, V.I., and Jones, J.D. (1997). AtDMC1, the Arabidopsis homologue of the yeast DMC1 gene:
645 characterization, transposon-induced allelic variation and meiosis-associated expression. Plant J 11, 1-14.
646 Komis, G., Luptovciak, I., Ovecka, M., Samakovli, D., Samajova, O., and Samaj, J. (2017). Katanin Effects on
647 Dynamics of Cortical Microtubules and Mitotic Arrays in Arabidopsis thaliana Revealed by Advanced Live-Cell
648 Imaging. Front Plant Sci 8, 866.
649 Kuchen, E.E., Fox, S., de Reuille, P.B., Kennaway, R., Bensmihen, S., Avondo, J., Calder, G.M., Southam, P.,
650 Robinson, S., Bangham, A., *et al*. (2012). Generation of leaf shape through early patterns of growth and tissue
651 polarity. Science 335, 1092-1096.
652 Landrein, B., Kiss, A., Sassi, M., Chauvet, A., Das, P., Cortizo, M., Laufs, P., Takeda, S., Aida, M., Traas, J., et al.
653 (2015). Mechanical stress contributes to the expression of the STM homeobox gene in Arabidopsis shoot
654 meristems. Elife 4, e07811.
655 Long, Y., Cheddadi, I., Mosca, G., Mirabet, V., Dumond, M., Kiss, A., Traas, J., Godin, C., and Boudaoud, A. (2020).
656 Cellular Heterogeneity in Pressure and Growth Emerges from Tissue Topology and Geometry. Curr Biol 30, 1504-
657 1516 e1508.
658 Lora, J., Herrero, M., Tucker, M.R., and Hormaza, J.I. (2017). The transition from somatic to germline identity shows
659 conserved and specialized features during angiosperm evolution. New Phytol 216, 495-509.
660 Lora, J., Yang, X., and Tucker, M.R. (2019). Establishing a framework for female germline initiation in the plant
661 ovule. J Exp Bot 70, 2937-2949.
662 Luptovciak, I., Komis, G., Takac, T., Ovecka, M., and Samaj, J. (2017). Katanin: A Sword Cutting Microtubules for
663 Cellular, Developmental, and Physiological Purposes. Front Plant Sci 8, 1982.
664 Luptovciak, I., Samakovli, D., Komis, G., and Samaj, J. (2017). KATANIN 1 Is Essential for Embryogenesis and Seed
665 Formation in Arabidopsis. Front Plant Sci 8, 728.
666 Mendocilla-Sato, E.B., C. (2017). Analysis of 3D Cellular Organization of Fixed Plant Tissues Using a User-guided
667 Platform for Image Segmentation. Bio-protocols 7, e2355.
668 Mosca, G.A., M.; Strauss, S.; Runions, R.; Sapala, A.; Smith, R.S. (2018). Modeling plant tissue growth and cell
669 division. In Mathematical Modelling in Plant Biology. (Springer, Cham), pp. 107-138.

670 Nonomura, K., Miyoshi, K., Eiguchi, M., Suzuki, T., Miyao, A., Hirochika, H., and Kurata, N. (2003). The MSP1 gene is
671 necessary to restrict the number of cells entering into male and female sporogenesis and to initiate anther wall
672 formation in rice. Plant Cell 15, 1728-1739.
673 Olmedo-Monfil, V., Duran-Figueroa, N., Arteaga-Vazquez, M., Demesa-Arevalo, E., Autran, D., Grimanelli, D.,
674 Slotkin, R.K., Martienssen, R.A., and Vielle-Calzada, J.P. (2010). Control of female gamete formation by a small RNA
675 pathway in Arabidopsis. Nature 464, 628-632.
676 Ovefçka M, L.I., Komis G, ≈†amajov√° O, Samakovli D, ≈†amaj J. (2020). Spatiotemporal Pattern of Ectopic Cell
677 Divisions Contribute to Mis-Shaped Phenotype of Primary and Lateral Roots of katanin1 Mutant. Front. Plant Sci.
678 Paluch, E., and Heisenberg, C.P. (2009). Biology and physics of cell shape changes in development. Curr Biol 19,
679 R790-799.
680 Panteris, E., Adamakis, I.D., Voulgari, G., and Papadopoulou, G. (2011). A role for katanin in plant cell division:
681 microtubule organization in dividing root cells of fra2 and lue1Arabidopsis thaliana mutants. Cytoskeleton
682 (Hoboken) 68, 401-413.
683 Peaucelle, A., Braybrook, S.A., Le Guillou, L., Bron, E., Kuhlemeier, C., and Hofte, H. (2011). Pectin-induced changes
684 in cell wall mechanics underlie organ initiation in Arabidopsis. Curr Biol 21, 1720-1726.
685 Pinto, S.C., Mendes, M.A., Coimbra, S., and Tucker, M.R. (2019). Revisiting the Female Germline and Its Expanding
686 Toolbox. Trends Plant Sci 24, 455-467.
687 Pujadas, E., and Feinberg, A.P. (2012). Regulated noise in the epigenetic landscape of development and disease.
688 Cell 148, 1123-1131.
689 Reik, W., and Surani, M.A. (2015). Germline and Pluripotent Stem Cells. Cold Spring Harb Perspect Biol 7.
690 Ren, H., Dang, X., Cai, X., Yu, P., Li, Y., Zhang, S., Liu, M., Chen, B., and Lin, D. (2017). Spatio-temporal orientation of
691 microtubules controls conical cell shape in Arabidopsis thaliana petals. PLoS Genet 13, e1006851.
692 Rodriguez, E.K., Hoger, A., and McCulloch, A.D. (1994). Stress-dependent finite growth in soft elastic tissues. J
693 Biomech 27, 455-467.
694 Rodriguez-Leal, D., Leon-Martinez, G., Abad-Vivero, U., and Vielle-Calzada, J.P. (2015). Natural variation in
695 epigenetic pathways affects the specification of female gamete precursors in Arabidopsis. Plant Cell 27, 1034-1045.
696 Savaldi-Goldstein, S., Peto, C., and Chory, J. (2007). The epidermis both drives and restricts plant shoot growth.
697 Nature 446, 199-202.
698 Scharloo (1991). Canalization: Genetic and Developmental Aspects. Annual Review of Ecology and Systematics 22,
699 65-93.
700 Schmidt, A., Schmid, M.W., and Grossniklaus, U. (2015). Plant germline formation: common concepts and
701 developmental flexibility in sexual and asexual reproduction. Development 142, 229-241.
702 Schmidt, A., Wuest, S.E., Vijverberg, K., Baroux, C., Kleen, D., and Grossniklaus, U. (2011). Transcriptome analysis of
703 the Arabidopsis megaspore mother cell uncovers the importance of RNA helicases for plant germline development.
704 PLoS Biol 9, e1001155.
705 Schneitz, K.; Hulskamp, M. and Pruitt, R.E. (1995). Wild-type ovule development in Arabidopsis thaliana: a light
706 microscope study of cleared whole-mount tissue. Plant Journal 7, 731-749.
707 She, W., Grimanelli, D., Rutowicz, K., Whitehead, M.W., Puzio, M., Kotlinski, M., Jerzmanowski, A., and Baroux, C.
708 (2013). Chromatin reprogramming during the somatic-to-reproductive cell fate transition in plants. Development
709 140, 4008-4019.
710 Sheridan, W.F., Avalkina, N.A., Shamrov, II, Batygina, T.B., and Golubovskaya, I.N. (1996). The mac1 gene:
711 controlling the commitment to the meiotic pathway in maize. Genetics 142, 1009-1020.
712 Sheridan, W.F., Golubeva, E.A., Abrhamova, L.I., and Golubovskaya, I.N. (1999). The mac1 mutation alters the
713 developmental fate of the hypodermal cells and their cellular progeny in the maize anther. Genetics 153, 933-941.
714 Sieber, P., Gheyselinck, J., Gross-Hardt, R., Laux, T., Grossniklaus, U., and Schneitz, K. (2004). Pattern formation
715 during early ovule development in Arabidopsis thaliana. Dev Biol 273, 321-334.

716 Skinner, D.J., Hill, T.A., and Gasser, C.S. (2004). Regulation of ovule development. Plant Cell 16 Suppl, S32-45.
717 Smith, R.S. (2009). Modeling plant morphogenesis and growth. In New Trends in the Physics and Mechanics of
718 Biological Systems. Lecture Notes of the Les Houches Summer School., Volume 22, M.G. Ben Amar, A.; M√°ller,
719 M.M.; Cugliandolo, L., ed. (Oxford: Oxford University Press).
720 Strzalka, W., and Ziemienowicz, A. (2011). Proliferating cell nuclear antigen (PCNA): a key factor in DNA replication
721 and cell cycle regulation. Ann Bot 107, 1127-1140.
722 Su, Z., Zhao, L., Zhao, Y., Li, S., Won, S., Cai, H., Wang, L., Li, Z., Chen, P., Qin, Y., *et al.* (2017). The THO Complex
723 Non-Cell-Autonomously Represses Female Germline Specification through the TAS3-ARF3 Module. Curr Biol 27,
724 1597-1609 e1592.
725 Su, Z. ; Wang, N. ; Hou, Z. ; Li, B. ; Li, D. ; Liu, Y. ; Cai, H. ; Qin, Y. and Chen X. (2020). Regulation of Female Germline
726 Specification via Small RNA Mobility in Arabidopsis. Plant Cell. Jul 23:tpc.00126.2020. doi: 10.1105/tpc.20.00126.
727 Online ahead of print.
728 Truernit, E., Bauby, H., Dubreucq, B., Grandjean, O., Runions, J., Barthelemy, J., and Palauqui, J.C. (2008). High-
729 resolution whole-mount imaging of three-dimensional tissue organization and gene expression enables the study
730 of Phloem development and structure in Arabidopsis. Plant Cell 20, 1494-1503.
731 Tucker, M.R., Okada, T., Hu, Y., Scholefield, A., Taylor, J.M., and Koltunow, A.M. (2012). Somatic small RNA
732 pathways promote the mitotic events of megagametogenesis during female reproductive development in
733 Arabidopsis. Development 139, 1399-1404.
734 Ubeda-Tomas, S., Federici, F., Casimiro, I., Beemster, G.T., Bhalerao, R., Swarup, R., Doerner, P., Haseloff, J., and
735 Bennett, M.J. (2009). Gibberellin signaling in the endodermis controls Arabidopsis root meristem size. Curr Biol 19,
736 1194-1199.
737 Uyttewaal, M., Burian, A., Alim, K., Landrein, B., Borowska-Wykret, D., Dedieu, A., Peaucelle, A., Ludynia, M., Traas,
738 J., Boudaoud, A., *et al*. (2012). Mechanical stress acts via katanin to amplify differences in growth rate between
739 adjacent cells in Arabidopsis. Cell 149, 439-451.
740 Waddington, C.H. (1942). Canalization of development and the inheritance of acquired characters. Nature, 563-
741 565.
742 Whitewoods, C.D., and Coen, E. (2017). Growth and Development of Three-Dimensional Plant Form. Curr Biol 27,
743 R910-R918.
744 Wightman, R., Chomicki, G., Kumar, M., Carr, P., and Turner, S.R. (2013). SPIRAL2 determines plant microtubule
745 organization by modulating microtubule severing. Curr Biol 23, 1902-1907.
746 Wolny, A., Cerrone, L., Vijayan, A., Tofanelli, R., Vilches Barro, A., Louveaux, M., Wenzl, C., Steigleder, S., Pape, C.,
747 Bailoni, A., *et al.* (2020). Accurate and Versatile 3D Segmentation of Plant Tissues at Cellular Resolution. bioRxiv,
748 2020.2001.2017.910562.
749 Yokoyama, R., Hirakawa, T., Hayashi, S., Sakamoto, T., and Matsunaga, S. (2016). Dynamics of plant DNA
750 replication based on PCNA visualization. Sci Rep 6, 29657.
751 Zhang, Q., Fishel, E., Bertroche, T., and Dixit, R. (2013). Microtubule severing at crossover sites by katanin
752 generates ordered cortical microtubule arrays in Arabidopsis. Curr Biol 23, 2191-2195.
753 Zhao, X., Bramsiepe, J., Van Durme, M., Komaki, S., Prusicki, M.A., Maruyama, D., Forner, J., Medzihradszky, A.,
754 Wijnker, E., Harashima, H., *et al.* (2017). RETINOBLASTOMA RELATED1 mediates germline entry in Arabidopsis.
755 Science 356.
756 Zhao, X., de Palma, J., Oane, R., Gamuyao, R., Luo, M., Chaudhury, A., Herve, P., Xue, Q., and Bennett, J. (2008).
757 OsTDL1A binds to the LRR domain of rice receptor kinase MSP1, and is required to limit sporocyte numbers. Plant J
758 54, 375-387.

Figure 1

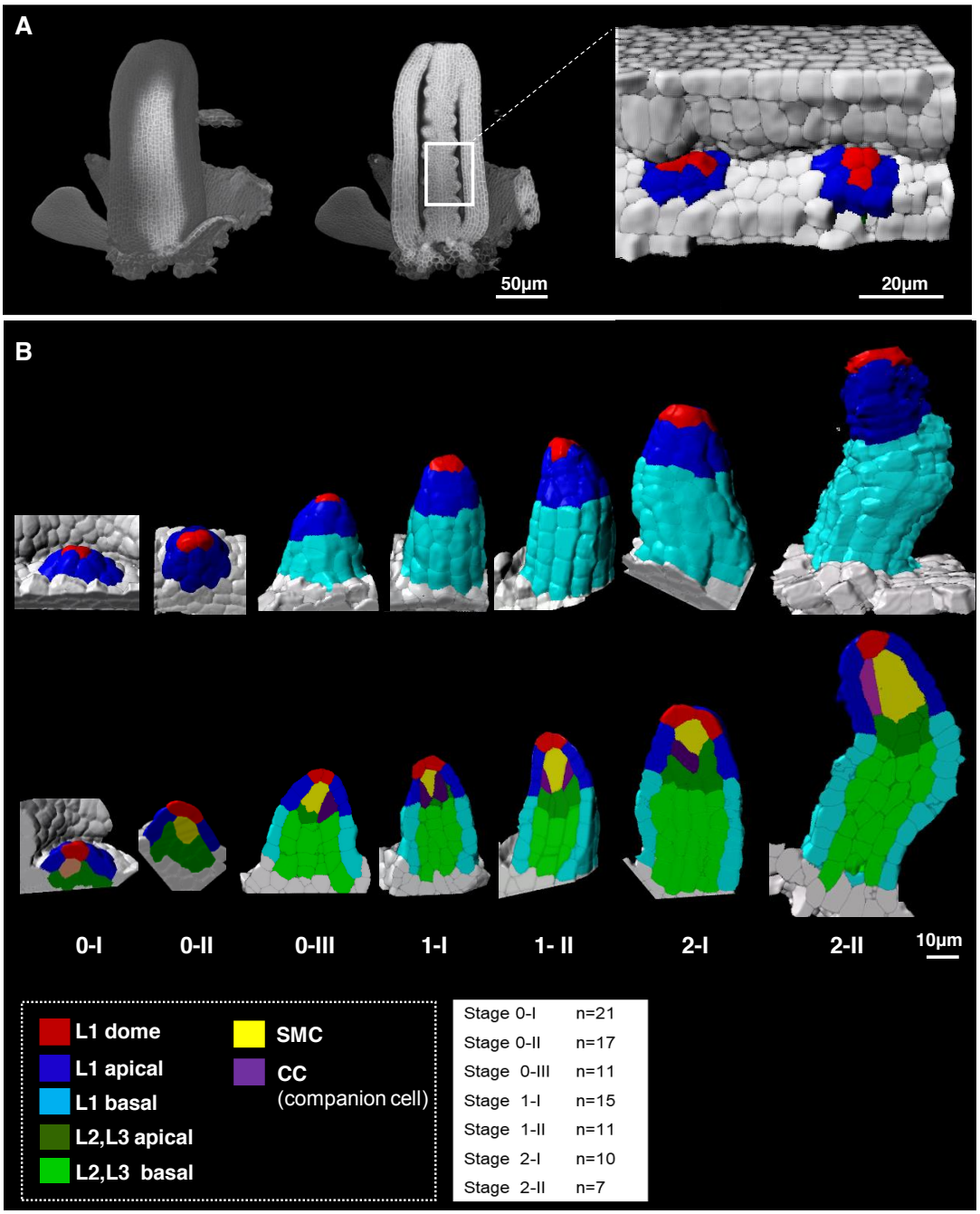

Figure 1. Reference set of 3D segmented images capturing Arabidopsis ovule primordium growth at cellular-resolution.

(A) 3D reconstruction of a whole gynoecium stained with PS-PI (cell wall dye) and visualized by CSLM. The cross section allows showing the nascent ovule primordia attached to the placenta.
(B) Ovule primordium developmental stages (0-I to 2-II) and organ viewpoints (domains) defined for the 3D quantitative analysis. All segmented data can be analyzed by an interactive interface named OvuleViz. See also Figure S1A-C.
n= number of ovules analyzed. Segmented images for all developmental stages are provided in Data S1. See also Figure S1 D-E, STAR Methods.

	0-I			0-II			0-III		
Cells above placenta*	2.5	(±3.5)	(n=21)	3.6	(±0.5)	(n=17)	5.9	(±1.0)	(n=11)
range (min-max)	2	-	3	3	-	4	5	-	8
total # cells	28	(±5.7)	(n=21)	38	(±8.0)	(n=17)	80	(±8.4)	(n=11)
width (µm) (W)	23	(±3.5)		26.3	(±2.4)		28.0	(±3.1)	
height (µm) (H)	5.3	(±1.2)		11.9	(±2.1)		22.5	(±3.6)	
H:W ratio	0.2	(±0.04)	(n=13)	0.45	(±0.06)	(n=14)	0.8	(±0.12)	(n=8)

	1-I			1-II		
cells above placenta*	7.3	(±1.3)	(n=15)	9.7	(±1.0)	(n=11)
range (min-max)	6	-	10	8	-	11
total # cells	105	(±10.6)	(n=15)	128	(±18.0)	(n=11)
width (µm) (W)	27	(±2.0)		27.8	(±3.5)	
height (µm) (H)	30	(±2.8)		39	(±5.9)	
H:W ratio	1.1	(±0.10)	(n=6)	1.4	(±0.22)	(n=8)

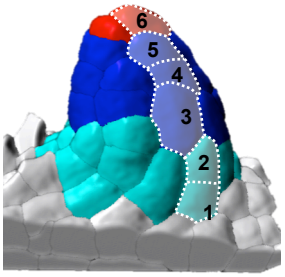

	2-I			2-II		
cells above placenta*	10	(±1.1)	(n=10)	12.6	(±1.0)	(n=7)
range (min-max)	9	-	12	11	-	14
total # cells	151	(±18.9)	(n=10)	165	(±19.8)	(n=7)

* scoring the length of L1 cell file above placenta

Table 1. Classification criteria of Arabidopsis ovule primordia

The table summarizes general characteristics of ovule primordia per stage: cell “layers” above the placenta scored as the number of L1 cells in a cell file drawn from the basis to the top, range thereof, total cell number, ovule shape including heigth, width, aspect ratio.

Figure 2

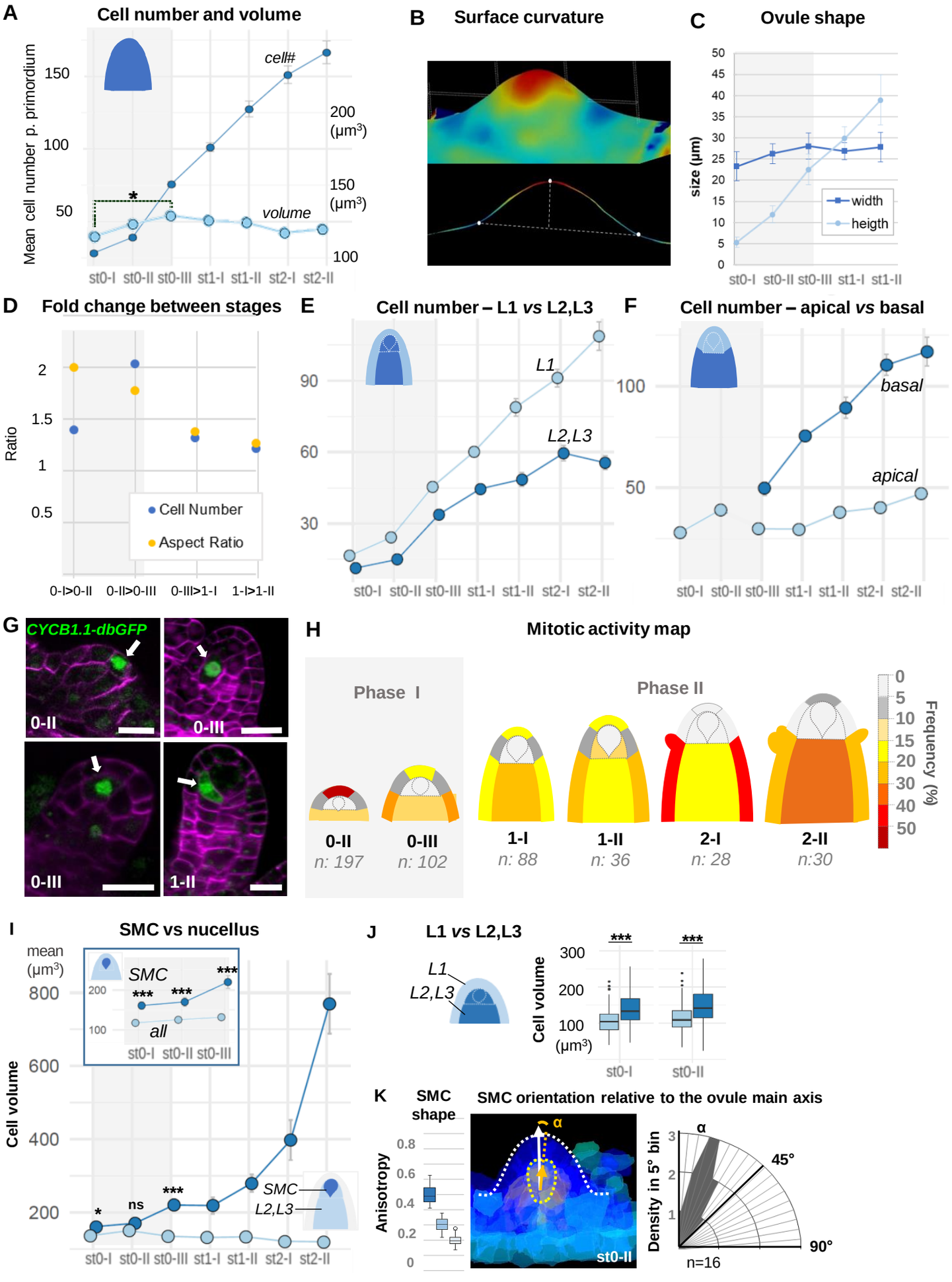
A
Cell number and volume
Mean cell number p. primordium
cell#
volume
200 (µm³)
150 (µm³)
100
st0-I st0-II st0-III st1-I st1-II st2-I st2-II
B
Surface curvature
C
Ovule shape
size (µm)
width
heigth
st0-I st0-II st0-III st1-I st1-II
D
Fold change between stages
Ratio
Cell Number
Aspect Ratio
0-I>0-II 0-II>0-III 0-III>1-I 1-I>1-II
E
Cell number – L1 vs L2,L3
L1
L2,L3
st0-I st0-II st0-III st1-I st1-II st2-I st2-II
F
Cell number – apical vs basal
basal
apical
st0-I st0-II st0-III st1-I st1-II st2-I st2-II
G
CYCB1.1-dbGFP
0-II
0-III
0-III
1-II
H
Mitotic activity map
Phase I
Phase II
0-II n: 197
0-III n: 102
1-I n: 88
1-II n: 36
2-I n: 28
2-II n:30
Frequency (%)
I
SMC vs nucellus
mean (µm³)
Cell volume
SMC
all
st0-I st0-II st0-III
SMC
L2,L3
st0-I st0-II st0-III st1-I st1-II st2-I st2-II
J
L1 vs L2,L3
L1
L2,L3
Cell volume
st0-I st0-II
K
SMC shape
Anisotropy
SMC orientation relative to the ovule main axis
st0-II
Density in 5° bin
45°
90°
n=16

Figure 2. Ovule primordium morphogenesis involves domain-specific cell division and anisotropic cell growth patterns.

(A) Mean cell number *per* ovule increases mainly during stages 0-I to 0-III (Phase I), whereas cell volume *per* ovule remains constant on average across primordium development (stages 0-I to 2-II).
(B) Representative image of a continuous surface of an ovule primordium mesh and its projected median plane. Dashed lines indicate the minimal and maximal curvature points used to measure organ height and width. Color scale: minimal curvature mm-1 (see also Figure S2B).
(C) Anisotropic organ growth during Phase I and until stage 1-II. Mean width and height quantifications *per* stage.
(D) Phase I captures a distinct growth dynamic compared to Phase II. Fold-change of cell number and aspect ratio between stages are plotted.
(E) Mean cell number is increased at the L1 *versus* L2,L3 layers across developmental stages.
(F) Mean cell number is increased in the basal *versus* apical domain across developmental stages.
(G) Representative images of ovule primordia expressing the M-phase reporter *pCYCB1.1::db-GFP.* White arrows indicate dividing cells. Magenta signal: Renaissance SR2200 cell-wall label. Scale bar: 10µm.
(H) Domain-specific map of mitotic activity during ovule primordium development, scored using the *pCYCB1.1::db-GFP* reporter. The frequency of mitoses was calculated *per* ovule domain at each developmental stage and color-coded as indicated in the bar (right). n: total number of scored ovules.
(I) Mean SMC volume (dark blue) is significantly increased as compared to L2,L3 cells (pale blue) from stage 0-III onward, on even at earlier stages as compared to all other cells (inset).
(J) Mean cell volume is increased in L2,L3 cells as compared to L1 cells, at the two early developmental stages (st0-I, st0-III).
(K) The SMC consistently displays anisotropic shape with main axis of elongation aligned with ovule growth axis. The SMC anisotropy index (boxplot, left; stage 0-II, n=16 ovules) was calculated from the Maximum (dark blue), Minimum (light blue) and Medium (medium blue) covariance matrix eigenvalues, computed from 3D segmented cells (see Figure S2G). Image (middle): illustration of the SMC main anisotropy axis (orange arrow) related by an angle 'alpha' to the main axis of the ovule primordium (white arrow), stage 0-II. Radar plot (right): 'alpha' angle measured on z projections for n=16 ovule primordia at stage 0-II. See also Star Methods.
Error bars: Standard errors to the mean. Differences between cell types or primordium domains were assessed using a two-tailed Man Whitney U test in (A) and (I); a two-tailed Wilcoxon signed rank test in (J). *p≤0.05, **p≤0.01, ***p≤0.001. See also Figure S2, Data S2, STAR Methods.

Modeling hypotheses		Models							
		1	2	3	4	5	6	7	8
Growth anisotropy		●	●	-	●	●	●	●	●
Material anisotropy		●	-	○	○	○	○	○	○
Passive Strain-based relaxation		●	●	●	●	●	●	●	-
Signal-based growth									
Distribution	L1 only	-	-	-	-	-	●	-	-
	Inner tissue only (pit-shape)	-	-	-	-	-	-	●	-
	L1 + inner tissue (pit-shape)	●	●	●	-	●	-	-	●
	L1 + inner tissue (broad distribution)	-	-	-	●	-	-	-	-
Fixed high concentration	L1 only	-	-	-	-	●	●	-	-
	Inner tissue only	-	-	-	-	-	-	●	-
	L1 + inner tissue	●	●	●	●	-	-	-	●

Table 2. Hypotheses used to generate the mass-spring (MS) and continuous Finite Element Method (FEM) based simulations

Several growth and mechanical hypotheses were listed at start of modelling. To evaluate their effect on primordium growth each hypothesis was excluded (-) in at least one scenario. The FEM and mass-spring (MS) models presented in Figure 3 and S3 are numbered according to the scenarios (1-8) in the table. Since it is not possible for MS to simulate material anisotropy, Model 1 was only tested with FEM. Empty dots for "Material anisotropy" were considered only for the FEM models. See also STAR Methods.

Figure 3

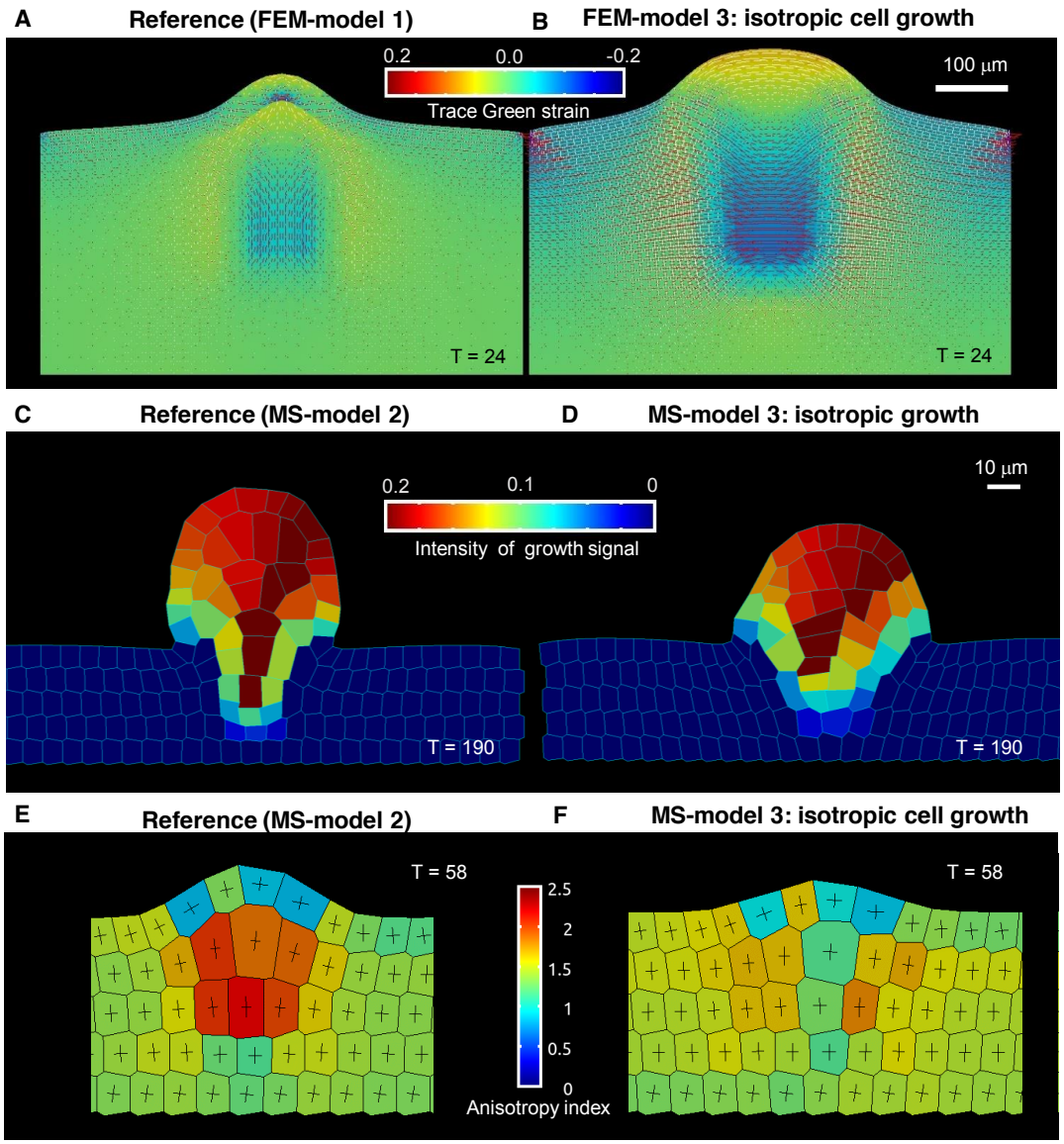

Figure 3. Mechanical and cell-based 2D simulation models of ovule primordium development predict that ovule shape depends on cell growth anisotropy.

(A) Reference model for FEM-based simulation of ovule primordium growth. Growth stability is reached at T=24. The fine lines indicate principal strain directions (white: expansive strain, red: compressive strain).

(B) FEM-based simulation omitting the anisotropic growth parameter (FEM-model 3) showing abnormal ovule dome shape at T=24.

(C) Reference model for Mass Spring (MS) cell-based simulation of ovule primordium growth. Growth stability is reached at T=190.

(D) MS cell-based simulation with isotropic cell growth (MS-model 3), showing enlarged apex and dome shape and abnormal cell division planes in L1, at T=190.

(E) Reference model for MS cell-based simulation showing emergence of L2 cell anisotropy at T=58.

(F) MS cell-based simulation MS-Model 3 (see Table 2) showing reduced L2 cells anisotropy at T=58.

Heatmaps: strain levels (A-B), growth signal intensity (C-D), 2D anisotropy index (E-F). See also Figure S3, Table 2 for model hypotheses and STAR Methods.

Figure 4

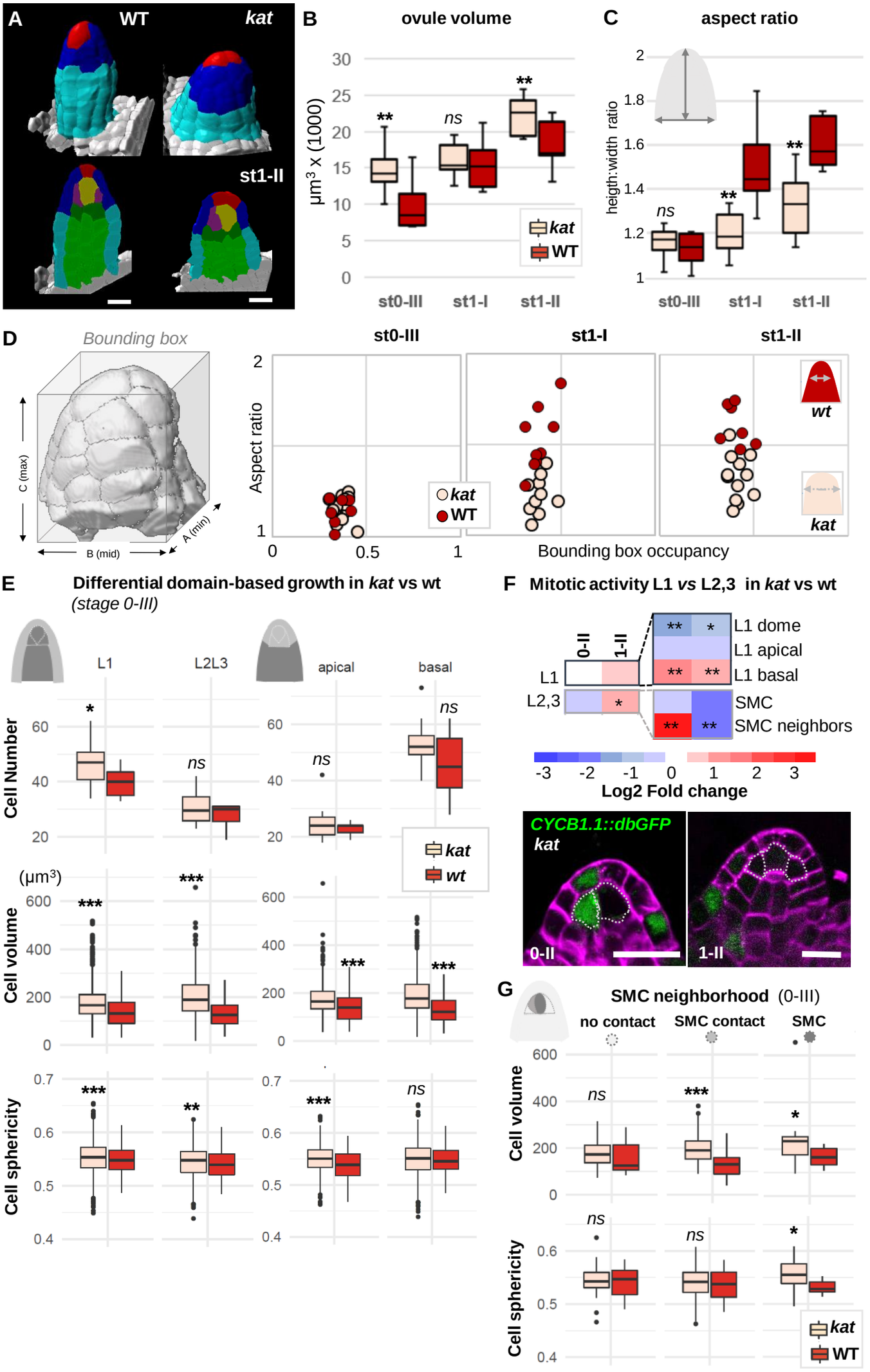
A
WT
kat
st1-II
B
ovule volume
µm³ x (1000)
kat
WT
st0-III
st1-I
st1-II
C
aspect ratio
heigth:width ratio
D
Bounding box
C (max)
B (mid)
A (min)
st0-III
st1-I
st1-II
Aspect ratio
Bounding box occupancy
wt
kat
E
Differential domain-based growth in kat vs wt
(stage 0-III)
L1
L2L3
apical
basal
Cell Number
Cell volume
(µm³)
Cell sphericity
kat
wt
F
Mitotic activity L1 vs L2,3 in kat vs wt
0-II
1-II
L1
L2,3
L1 dome
L1 apical
L1 basal
SMC
SMC neighbors
Log2 Fold change
CYCB1.1::dbGFP
kat
0-II
1-II
G
SMC neighborhood (0-III)
no contact
SMC contact
SMC
Cell volume
Cell sphericity
kat
WT

Figure 4. *katanin* mutants show a distinct ovule primordium architecture, primarily through altered cell division patterns.

Comparison between wild-type (WT, Ws-4 accession) and *katanin (kat, bot1-7* allele*)* ovule primordia unless indicated otherwise.

(A) 3D segmented images at stage 1-II. External organ view (top) and longitudinal sections (bottom) are shown. Scale bar 10µm. See Data S2a for full datasets.

(B-D) Morphological difference between WT and *kat* primordia measured by their volume (B), the aspect ratio (C), and aspect ratio to bounding box occupancy relationship (D). D, Left: scheme representing the bounding box capturing the primordium's 3D surface. See also Figure S4A.

(E) Quantification of cell number, cell volume, and sphericity in comparisons of L1 *versus* L2,L3 and apical *versus* basal domains at stage 0-III. See also Figure S4C.

(F) Mitotic activity domains are altered in *kat* primordia. Top: Heatmap of Log2 fold change of mitotic activity in the *kat* mutant (*lue1* allele) *versus* WT (Col-0) *per* domain, at two developmental stages. The frequency of mitoses was measured as in Figure 2. Full maps of mitotic activity in different mutant alleles are shown Figure S4E. Bottom: representative images of *kat* primordia (*lue1* allele) expressing *pCYCB1.1::db-GFP*. Dashed lines mark L2 apical cells. Magenta signal: Renaissance SR2200 cell wall label. Scale bar 10µm.

(G) Mean cell volume and sphericity are increased in *katanin* L2 apical cells in contact with the SMC. SMC, cells in contact with the SMC, and cells not in direct contact with the SMC, are compared at stage 0-III.

Color code in all plots: Dark red: WT; Salmon: *kat* mutant. Error bars: standard error of the mean. Differences between WT and *kat* mutants in (B), (C), (E), and (G) were assessed using a Mann Whitney U test; a two-tailed Fischer's exact test was used in (F). P values: *p≤0.05, **p≤0.01, ***p≤0.001. See also Figure S4 and Data S4.

Figure 5

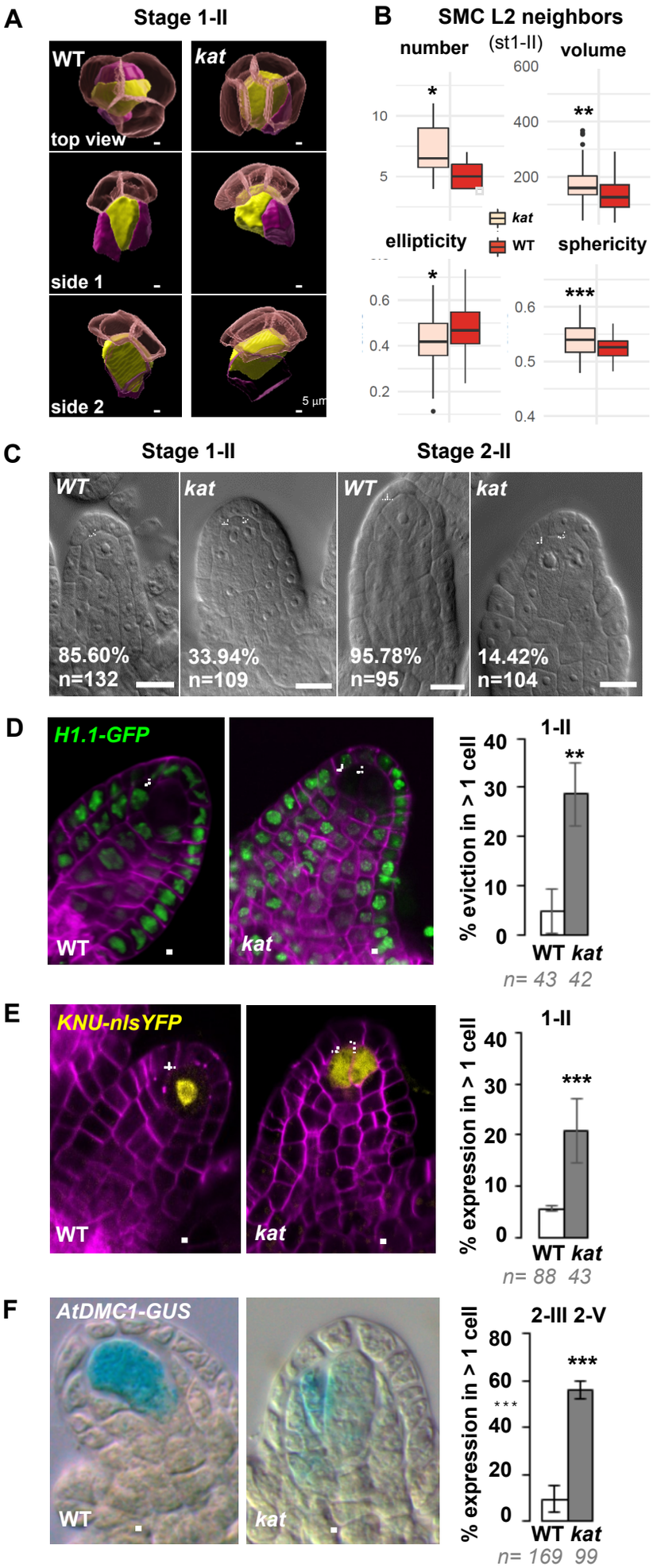
A
Stage 1-II
WT
kat
top view
side 1
side 2
5 µm
B
SMC L2 neighbors
number
(st1-II)
volume
ellipticity
sphericity
kat
WT
C
Stage 1-II
Stage 2-II
WT
kat
85.60%
n=132
33.94%
n=109
95.78%
n=95
14.42%
n=104
D
H1.1-GFP
WT
kat
1-II
% eviction in > 1 cell
n= 43 42
E
KNU-nlsYFP
WT
kat
1-II
% expression in > 1 cell
n= 88 43
F
AtDMC1-GUS
WT
kat
2-III 2-V
% expression in > 1 cell
n= 169 99

Figure 5. Altered ovule primordium architecture in *katanin* mutants is associated with multiple SMCs.

(A) SMCs lose their typical pear shape in *katanin* (*kat*) mutants. 3D images of the apical-most cells according to top and side views as indicated, showing the SMC (yellow), SMC neighbors (purple), and the L1 dome (transparent red).

(B) Differential properties of L2,L3 apical domain cells (SMC and SMC neighbors) in terms of cell number, mean cell volume, ellipticity, and sphericity at stage 1-II. See also Figure S5A and Data S4b.

(C) Representative images of cleared wild-type (WT) and *kat* ovule primordia. The % indicate the frequency of ovules showing one SMC for WT primordia, or multiple SMC candidates (dashed lines) for *kat* primordia.

(D-E) Representative images and quantification of SMC fate markers in WT and *kat* primordia: eviction of the *H1.1::H1.1-GFP* marker (green, D) and ectopic expression of *KNU::nls-YFP* (yellow, E) in more than one cell *per* primordia, are increased in *kat* primordia. See also Figure S5B.

(F) The meiotic marker *AtDMC1::GUS* is ectopically expressed in *kat* ovules.

Mutant alleles: *bot1-7* (A-B), *mad5* (C-E), *lue1* (F). Additional *kat* alleles, stages and detailed quantifications are presented Figure S5 and Data S5. Magenta signal in (B) and (C): Renaissance SR2200 cell wall label. Scale bars for (C), (D) and (E): 10µm. n: number of ovules scored. Error bar: standard error of the mean. Differences between WT and *kat* genotypes were assessed using a Mann Whitney U test in (B), and a two-tailed Fischer's exact test in (D), (E), and (F). P values: *p≤0.05, **p≤0.01, ***p≤0.001. See also Figure S5 and Data S5.

Figure 6

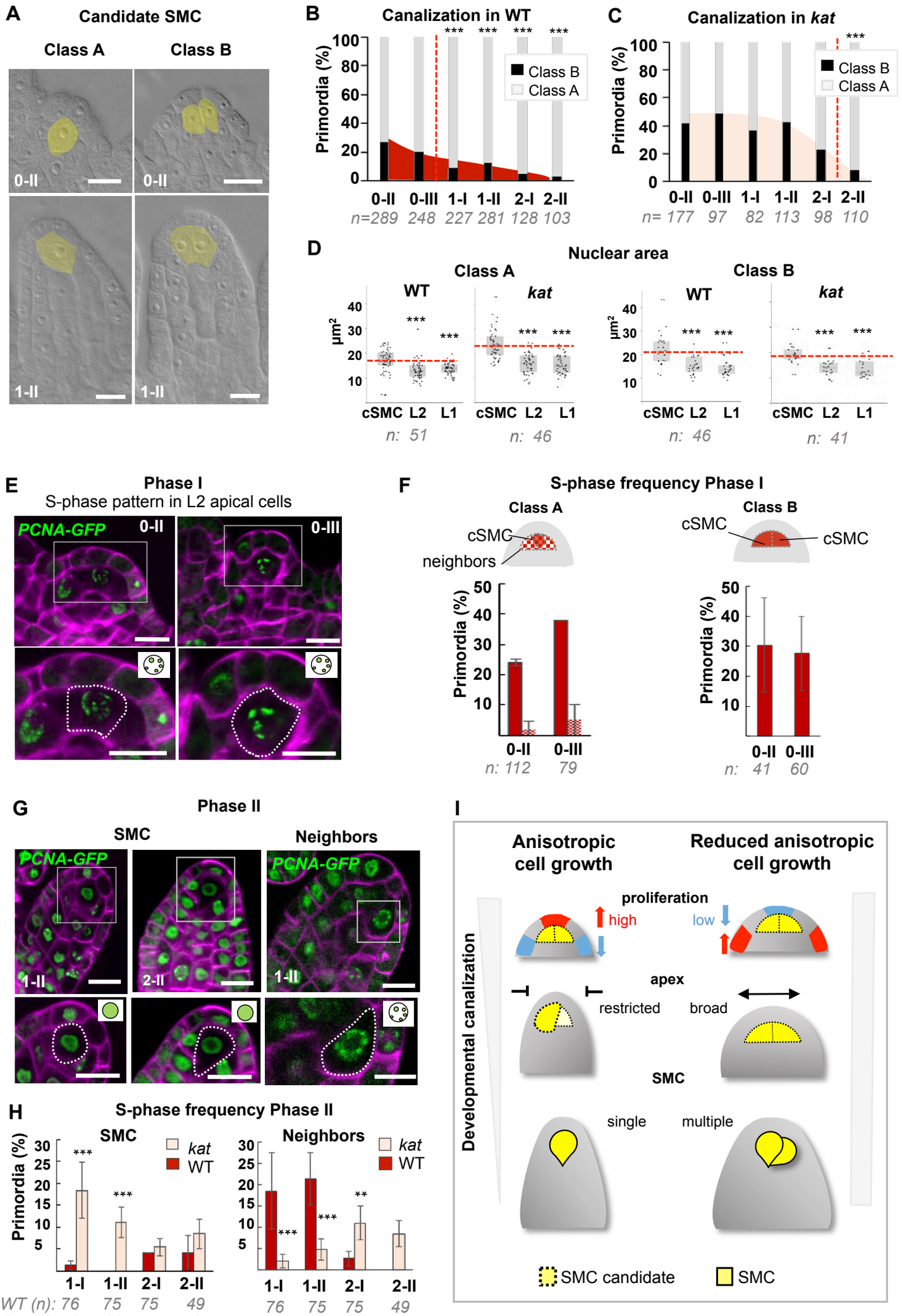
A
Candidate SMC
Class A
Class B
0-II
0-II
1-II
1-II
B
Canalization in WT
Primordia (%)
Class B
Class A
0-II 0-III 1-I 1-II 2-I 2-II
n=289 248 227 281 128 103
C
Canalization in kat
Primordia (%)
Class B
Class A
0-II 0-III 1-I 1-II 2-I 2-II
n= 177 97 82 113 98 110
D
Nuclear area
Class A
Class B
WT
kat
µm²
cSMC L2 L1
n: 51
n: 46
n: 46
n: 41
E
Phase I
S-phase pattern in L2 apical cells
PCNA-GFP
0-II
0-III
F
S-phase frequency Phase I
Class A
Class B
cSMC
neighbors
Primordia (%)
0-II 0-III
n: 112 79
n: 41 60
G
Phase II
SMC
Neighbors
PCNA-GFP
1-II
2-II
H
S-phase frequency Phase II
SMC
Neighbors
kat
WT
Primordia (%)
1-I 1-II 2-I 2-II
WT (n): 76 75 75 49
kat (n): 49 63 55 59
76 75 75 49
49 63 55 59
I
Anisotropic cell growth
Reduced anisotropic cell growth
proliferation
high
low
apex
restricted
broad
SMC
single
multiple
Developmental canalization
SMC candidate
SMC

Figure 6. The formation of a single SMC stems from a canalization process.

(A-B) In wild-type (WT) plants, ovule primordia harbour one (Class A) or occasionally two (Class B) SMC candidates with the frequency of class B gradually decreasing during development, reminiscent of developmental canalization. Typical images obtained by tissue clearing with SMC candidates highlighted in yellow (A) and plots showing the percentages of classes A and B (B). The frequency of class B ovules is significantly reduced from stage 1-I, suggesting that canalization (represented by the red dashed line) occur before that stage. The plot coloration is a visual aid only.

(C) Developmental canalization is delayed in *katanin* (*kat*) mutants (*mad5* allele). The proportion of class B ovules is significantly reduced from stage 2-II only. Quantifications for two additional mutants carrying *kat* alleles are presented Figure S6A. The plot coloration is a visual aid only.

(D) The candidate SMCs initially identified as enlarged cells consistently show an enlarged nucleus in both class A and class B primordia. Nuclear area is compared between the candidate SMCs (cSMC) and surrounding L2 and L1 cells (see Figure S6D and STAR Methods for further details). Box plots include jittered data points to visualize data variability. Red lines represent the median of cSMC nuclear area for comparison with other cell types. Equivalent quantifications for stage 0-III are presented in Figure S6F.

(E-F) During Phase I (stages 0-II, 0-III), S-phase is detected in candidate SMCs at higher frequency than in neighbors cells in class A ovules, and in both SMC candidates in class B ovules. Representative images of ovule primordia showing the speckled S-phase pattern of the *pPCNA1::PCNA:sGFP* reporter (green) (E). Magenta signal: Renaissance SR2200 cell wall label. Scale bar 10µm. Quantification of speckled S-phase pattern in the SMC candidate and L2 neighbors (class A ovules) or in both SMC candidates (class B) (F).

(G-H) During Phase II (stages 1-I to 2-II), in class A wild-type ovule primordia, SMC exits S-phase, and neighbors cells re-enter S-phase; while *katanin* primordia show the opposite pattern.. Representative images of class A ovule primordia primarily showing the nucleoplasmic G1/G2-phase pattern of *pPCNA1::PCNA:sGFP* in SMCs at stages 1-II (left panel) and 2-II (middle panel); and of the speckled S-phase pattern in neighbors cells (right panel). Quantification of speckled S-phase pattern in SMC candidates and neighbors in Phase II wild-type and *katanin* primordia (I). Representative images and quantifications of Phase I *katanin* primordia and of class B primodia are presented in Figure S6G-H. See also Figure 2H, S6E.

(I) Model for the role of *KATANIN* in primordium growth and SMC differentiation (graphical abstract). In WT primordia, SMC differentiation follows a developmental canalization process influenced by cell growth anisotropy that shapes the primordium apex. In *kat* mutants, reduced anisotropy modifies the cell proliferation pattern, enlarges the apex and the L2,L3 apical domain, leading to multiple SMC candidates (delayed canalization). We propose that ovule primordium shape, controlled by anisotropic cell growth, determines SMC singleness.

Images: scale bars : 10um. *Graphs*: n= total number of ovules. Error bar: standard error of the mean (F, I). Differences between cell types, domains, or genotypes as indicated in the graphs were assessed using Wilcoxon signed rank test in (D), and a two-tailed Fischer's exact test in B, C, F, and I. P values: *p≤0.05, **p≤0.01, ***p≤0.001. Quantifications for additional alleles and detailed quantifications are provided in Figure S6 and Data S6.